

Numerical Study of Horizontal Shear Instability Waves along Narrow Cold Frontal Rainbands

MASAYUKI KAWASHIMA

Institute of Low Temperature Science, Hokkaido University, Sapporo, Japan

(Manuscript received 6 July 2010, in final form 23 November 2010)

ABSTRACT

The effects of variations in low-level ambient vertical shear and horizontal shear on the alongfront variability of narrow cold frontal rainbands (NCFRs) that propagate into neutral and slightly unstable environments are investigated through a series of idealized cloud-resolving simulations.

In cases initialized with slightly unstable sounding and weak ambient cross-frontal vertical shears, core-gap structures of precipitation along NCFRs occur that are associated with wavelike disturbances that derive their kinetic energy mainly from the mean local vertical shear and buoyancy. However, over a wide range of environmental conditions, core-gap structures of precipitation occur because of the development of a horizontal shear instability (HSI) wave along the NCFRs.

The growth rate and amplitude of the HSI wave decrease significantly as the vertical shear of the ambient cross-front wind is reduced. These decreases are a consequence of the enhancement of the low-level local vertical shear immediately behind the leading edge. The strong local vertical shear acts to damp the vorticity edge wave on the cold air side of the shear zone, thereby suppressing the growth of the HSI wave through the interaction of the two vorticity edge waves. It is also noted that the initial wavelength of the HSI wave increases markedly with increasing horizontal shear. The local vertical shear around the leading edge is shown to damp long HSI waves more strongly than short waves, and the horizontal shear dependency of the wavelength is explained by the decrease in the magnitude of the vertical shear relative to that of the horizontal shear.

1. Introduction

The precipitation along a narrow cold frontal rainband (NCFR) that propagates into an environment of weak instability or neutral stability is often broken up into segments of intense precipitation called precipitation cores (PCs) separated by gaps of weaker rainfall, as first noted by James and Browning (1979) and Hobbs and Biswas (1979). The PCs are typically aligned at a clockwise angle with respect to the synoptic-scale cold front (e.g., Hobbs and Persson 1982; Parsons and Hobbs 1983a; Wakimoto and Bosart 2000). Horizontal shear instabilities (HSIs) along the leading edge of a cold front or their coupling with a convective instability have frequently been proposed as mechanisms that lead to the alongfront variability (AFV) of NCFRs (e.g., Matejka

1980; Hobbs and Persson 1982; Moore 1985, Carbone 1982; Parsons and Hobbs 1983b; Wakimoto and Bosart 2000; Smart and Browning 2009).

Numerous modeling studies indicate that the ambient vertical wind shear causes strong influence on the structure and evolution of squall lines (e.g., Hane 1973; Thorpe et al. 1982; Rotunno et al. 1988, hereafter RKW; Weisman et al. 1988; Fovell and Ogura 1989; Robe and Emanuel 2001). RKW found that the ability of the cold outflow from an old cell to lift environmental boundary layer air to its level of free convection (LFC) is enhanced with low-level shear, and they developed a widely cited theory that explains the squall-line strength and longevity in terms of a relative horizontal vorticity balance between the circulation associated with the cold pool and that associated with the environmental wind shear (often called RKW theory). Modeling and observational studies have also identified the importance of the low-level vertical shear in modulating the structure of NCFRs. Parsons (1992) showed, in a series of two-dimensional numerical simulations, that the dependence of the neutrally

Corresponding author address: Dr. Masayuki Kawashima, Institute of Low Temperature Science, Hokkaido University, Sapporo 060-0819, Japan.
E-mail: kawashima@lowtem.hokudai.ac.jp

buoyant frontal updraft associated with an NCFR on vertical shear is consistent with that predicted by RKW theory. Jorgensen et al. (2003) investigated the variation of the precipitation and updraft structure of a strong NCFR using Doppler radar data. They found that variations in the strength of the low-level vertical shear of ambient flow caused a systematic variation of the updraft tilt along the length of PCs and in gap regions that is consistent with RKW theory. However, most of the previous studies on AFVs of NCFRs were case studies, and no attempts have been made to systematically investigate the effect of ambient vertical shear through idealized numerical simulations.

Kawashima (2007, hereafter K07) recently investigated the mechanism responsible for core-gap structures of precipitation along NCFRs through a series of idealized simulations of cold fronts forced by shearing deformation. He attributed the formation of PCs to wavelike disturbances within slanted frontal updrafts, which derive their kinetic energy mainly from the kinetic energy of the vertical shear flow and the buoyancy. It was also shown in K07 that the structure of PCs changes from those oriented clockwise to the general orientation of the surface cold front (SCF) to those oriented counterclockwise to the SCF as convective available potential energy (CAPE) in the prefrontal environment increases. However, all simulations in K07 were initialized using an ambient cross-front wind with a rather weak low-level vertical shear, which caused mean frontal updrafts to lean significantly back over the cold air. This raises a question about the generality and applicability of the mechanism proposed by K07, since typical environments of cold fronts are strongly baroclinic and therefore strongly sheared (e.g., Houze et al. 1976). In fact, some discrepancies were noted by K07 between observations and his simulation results. For example, Doppler radar observations of typical PCs that were oriented clockwise to the SCF revealed that the PCs were related systematically to the distortions of the SCF that would be a manifestation of HSI (e.g., Hobbs and Persson 1982; Wakimoto and Bosart 2000). On the other hand, the distortion of the SCF was weak and characteristic features of HSI were not recognized in K07's simulations that produced such PCs. Furthermore, while Parsons and Hobbs (1983a) reported a case in which typical PCs developed along an NCFR whose prefrontal environment was absolutely stable (see their Figs. 10 and 11), a certain amount of CAPE was required for the formation of typical PCs in K07's simulations.

Lee and Wilhelmson (1997a, hereafter LW97a) investigated mesocyclone development along numerically simulated thunderstorm outflow boundary. They noted that the growth of HSIs that could eventually form mesocyclones is either delayed or completely absent as the

low-level environmental vertical shear normal to the cold outflow leading edge is reduced from an optimal value. Although the horizontal shear zones associated with cold outflows simulated by LW97a were much narrower compared with that for typical NCFRs, their results suggest that the weak ambient vertical shear condition adopted in K07 was not conducive to the growth of HSIs along NCFRs.

The objective of this paper is to systematically investigate the sensitivity of AFV of NCFRs to variations in the environmental characteristics through a series of idealized simulations. The environmental characteristics studied include the ambient vertical shear of the cross-front wind, the atmospheric stability, and the strength of the leading edge horizontal wind shear. It is shown that core-gap structures of precipitation occur because of the development of an HSI wave along NCFRs under a wide range of environmental conditions. This paper focuses primarily on this type of AFV of NCFRs, which was not addressed in K07 but appears to be a more common type of AFV of NCFRs.

The outline of this paper is as follows. The model utilized in this study and the experimental design are described in section 2. In section 3, the impacts of variations in the vertical shear of ambient cross-front winds and the stability of the stratification on the AFVs of NCFRs are investigated. Section 4 offers an explanation concerning the suppression of HSI waves along NCFRs under weak ambient vertical shear conditions. Section 5 examines the impacts of variations in horizontal shear strength on HSI waves along NCFRs and discusses processes that account for a distinct relationship between the initial wavelength of the HSI wave and the horizontal shear strength identified in the simulations. Finally, the results are summarized in section 6.

2. Model description and experimental design

a. Model configuration

The model used in the present study is derived from the nonhydrostatic, moist shear–frontogenesis model described in K07. Several substantial modifications are made to systematically investigate the sensitivity of the AFV of an NCFR to variations in parameters of interest.

To investigate the sensitivity of the AFV of NCFR to variation in a parameter, it is desirable to keep other parameters unchanged. However, the use of the shear–frontogenesis model makes it difficult. For example, the variation of the ambient vertical shear of the cross-front wind entails the variation of the large-scale along-frontal gradient of temperature that could be advected by the alongfront wind through thermal wind relation. Thus,

a cold front simulated by the shear–frontogenesis model tends to be more intense and the prefrontal environment tends to be more unstable as the vertical shear increases. The horizontal shear at the leading edge of cold front can be varied by varying the Coriolis parameter in the model equations. However, the variation of the Coriolis parameter also entails the variation of the along-frontal gradient of temperature.

Around the leading edge of a mature, sharp cold front, where very large horizontal gradients in pressure, temperature, and wind exist within a few kilometers, the wind field is highly ageostrophic in the across- and even along-frontal directions (e.g., Parsons et al. 1987). In fact, an analysis of momentum equations for cold fronts simulated in K07 indicates that the Coriolis accelerations were smaller than advection terms and horizontal pressure gradient forces by approximately one order of magnitude around the leading edges (not shown). This indicates that the structure of the leading edge of a cold front can be simulated well without the Coriolis force. Thus, for the present study, the Coriolis effect is excluded and prescribed heat and moisture sinks are used to initialize cold fronts, relying upon findings that have shown that the structure of the leading edge of a cold front is similar to a that of a gravity current (e.g., Carbone 1982; Hobbs and Persson 1982; Parsons 1992). The exclusion of the Coriolis force allows us to vary parameters of interest almost independently, which makes the experiment simpler and easier to understand, though less realistic.

As in K07, the model is first integrated in its 2D (x, z) configuration for computational efficiency. Using the 2D model output at $t = 12$ h as the meridionally uniform initial condition, the model is then run in its 3D configuration for 8 h, within which time period AFVs are allowed to develop. The synoptic cold front is oriented in the north–south (y) direction. The experimental domain has dimensions of $L_x = 180$ km, $L_y = 300$ km, and $L_z = 10$ km. The east and west lateral boundaries are open, whereas the north and south boundaries are periodic. Rigid-lid top boundary conditions are applied together with a Rayleigh wave-absorbing layer over the uppermost 3 km. The model uses 180 grid points in the x direction, the central 120 of which comprise a fine mesh with a constant grid spacing of $\Delta x = 500$ m. A 60-km-wide stretch grid is placed on both sides of the fine mesh. The grid spacing in the y direction is constant at $\Delta y = 500$ m. Observations of NCFRs (e.g., Browning and Harrold 1970; Hobbs and Persson 1982; Wakimoto and Bosart 2000) indicate that the horizontal shear at the leading edge is on the order of 10^{-2} s^{-1} and the width of the wind shift zone is about 2–3 km. A horizontal grid spacing of 500 m is chosen because simulations with this grid size reproduce these characteristic values. The vertical grid

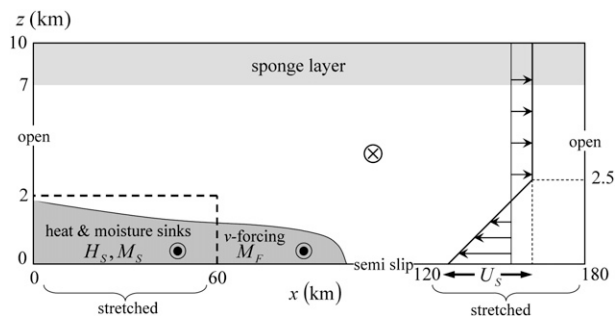


FIG. 1. A schematic of the configuration used to initialize 2D cold fronts. The dashed line at the left represents the location of H_s and M_s , and the shading indicates the cold air created by H_s and M_s . Arrows pointed out of the figure (southward) indicate the direction of M_F applied in the cold air. An arrow pointed into the figure denotes the direction of environmental alongfront wind (northward). The vertical profile of the initial cross-front wind is shown at the right. The model boundary conditions are also given.

stretches smoothly from $\Delta z = 100$ m in the lowest 1 km to 300 m at the top of the domain. A schematic of the 2D model configuration is shown in Fig. 1.

As in K07, a bulk aerodynamic surface friction parameterization similar to that employed by Wilhelmson and Chen (1982) is included to represent a semislip condition at the bottom. In this study, the initial wind field is assumed to be in balance with surface friction, and the drag is applied to perturbation velocities following Adlerman and Droegemeier (2002) to prevent significant modifications of the basic-state wind fields with time. The nondimensional drag coefficient C_d is set to 1.0×10^{-3} (over oceans). Subgrid-scale turbulence is parameterized using a Smagorinsky-type first-order closure (e.g., Lilly 1962). Fourth-order numerical damping is also applied in the horizontal, with the mixing coefficient set as $6.25 \times 10^7 \text{ m}^4 \text{ s}^{-1}$. All of the simulations reported herein are made with a Kessler-type warm-rain microphysics scheme for simplicity. The author performed several experiments with the ice microphysics scheme of Lin et al. (1983) and

TABLE 1. Thermodynamic profile diagnosis for the S0, S1, and S2 soundings. Listed are the lapse rate of potential temperature between 0 and 2 km, the strength of the potential instability [defined as the difference between surface and minimum θ_e ($\Delta\theta_e$)], the level of free convection (LFC), the level of neutral buoyancy (LNB), and the convective available potential energy (CAPE).

Sounding	$\partial\theta_0/\partial z$ for				
	$0 \leq z \leq 2$ km (K km $^{-1}$)	$\Delta\theta_e$ (K)	LFC (km)	LNB (km)	CAPE (J kg $^{-1}$)
S0	2.8 + 1.4z/2 km	—	—	—	—
S1	2.2 + 1.1z/2 km	1.56	0.61	2.42	31.4
S2	1.6 + 0.8z/2 km	3.74	0.43	3.07	120.6

confirmed that the inclusion of ice-phase microphysics does not impact the basic conclusions drawn herein.

b. Soundings

The initial environment is horizontally homogeneous in all of the 2D configuration runs in this study. The profiles

$$RH(z) = \begin{cases} 88 + 10 \tanh(z/0.8 \text{ km}) & \text{for } 0 \leq z \leq 2.0 \text{ km;} \\ 88 + 10 \tanh(2.0/0.8) - 0.01(z - 2.0 \text{ km}) & \text{for } z > 2.0 \text{ km.} \end{cases} \quad (1)$$

The lapse rate of potential temperature depends on altitude and is given by

$$\frac{\partial \theta_0}{\partial z} = \begin{cases} a + bz \text{ K km}^{-1} & \text{for } 0 \leq z \leq 2.0 \text{ km;} \\ 5.0 \text{ K km}^{-1} & \text{for } z > 2.0 \text{ km.} \end{cases} \quad (2)$$

The potential temperature at $z = 0$ km is 280 K. To investigate the sensitivity of AFV to variation in the atmospheric stability for various vertical and horizontal shear conditions, three different soundings, named S0, S1, and S2, are considered. The values of a and b and the basic properties for these soundings are summarized in Table 1, and profiles of θ_0 and the equivalent potential temperatures θ_e are shown in Fig. 2. The S0 sounding does not exhibit either potential or conditional instability [i.e., $\partial \theta_e / \partial z > 0$ throughout the entire depth and the level of free convection (LFC) does not exist], whereas the S1 and S2 soundings are both potentially and conditionally unstable at low levels.

Because the frontal updrafts considered in this study are rather shallow, cross-front wind profiles with constant positive shears confined to below $z = 2.5$ km—a condition used in many numerical studies (e.g., RKW; Fovell and Ogura 1989; Parsons 1992)—are examined (Fig. 3).

$$H_S(x, z, t) = \begin{cases} H_{S0}[1 + 10 \exp(-t/6000 \text{ s})] \text{ K s}^{-1} & \text{for } 0 \leq x \leq 60 \text{ km} \text{ and } 0 \leq z \leq 2.0 \text{ km;} \\ 0 & \text{otherwise.} \end{cases} \quad (3)$$

In the model the saturation mixing ratio q_s is given by

$$q_s = q_{s0} \exp\left(\frac{L\pi_0}{R_v T_0^2} \theta\right), \quad (4)$$

where q_{s0} is the saturation mixing ratio of the initial state, π_0 is the Exner pressure of the initial state, T_0 is the temperature of the initial state, and θ is the deviation of potential temperature from θ_0 . Thus $\partial q_s / \partial t$ can be related to $\partial \theta / \partial t$ and the heat sink as

of moisture and potential temperature θ_0 are defined by analytical expressions that loosely represent wintertime maritime prefrontal environments that are nearly saturated and almost neutral or slightly unstable to moist parcel ascents (e.g., Browning and Harrold 1970; Wang et al. 1983; Jorgensen et al. 2003). The relative humidity (RH; %) is given by

The difference between the zonal wind speeds at the surface and that at $z = 2.5$ km is denoted as U_S , and a series of experiments are conducted for $U_S = 5, 10, 15,$ and 20 m s^{-1} . Test simulations indicated that as U_S was increased beyond 20 m s^{-1} , a frontal updraft leaned downshear with height and a well-defined cold outflow boundary was not established. The vertical shear of the low-level cross-front wind used in K07 is almost the same as that for the $U_S = 5 \text{ m s}^{-1}$ profile. By subtracting a constant speed from u_0 , simulated NCFRs are maintained within the fine mesh. Test simulations also indicated that the variation in the vertical shear of v_0 exerts a relatively small influence on the structure of an AFV compared with that of u_0 ; thus, v_0 is not changed for all of the simulations presented herein. Considering the effect of surface friction, v_0 is decreased linearly from 22.5 m s^{-1} at $z = 0.75$ km to 15 m s^{-1} at $z = 0$ km.

c. Initialization of fronts

To create a quasi-steady cold air leading edge in the model domain, prescribed heat and moisture sink terms are added to prognostic equations for the potential temperature and the water vapor mixing ratio, respectively. The heat sink is given by

$$\frac{\partial q_s}{\partial t} = \frac{L\pi_0 q_{s0}}{R_v T_0^2} \left(\frac{\partial \theta}{\partial t}\right) = \frac{L\pi_0 q_{s0}}{R_v T_0^2} H_S. \quad (5)$$

Using above relationship, the moisture sink is given as

$$M_S(x, z, t) = \frac{RH(z)}{100} \left(\frac{\partial q_s}{\partial t}\right) = \frac{RH(z)}{100} \frac{L\pi_0 q_{s0}}{R_v T_0^2} H_S(x, z, t). \quad (6)$$

Based on the results of trial simulations, the values of H_{S0} are set to 0.18, 0.12, and 0.1 K h⁻¹ for simulations initialized with the S0, S1, and S2 soundings, respectively. The temperature differences across the SCFs created by these forcings are about 2 K, comparable with the observations by James and Browning (1979) and Hobbs and Persson (1982)

$$M_F(x, y, z, t) = \begin{cases} -C_M(u - u_0)[1 + 2 \exp(-t/18\,000\text{ s})] \text{ m s}^{-2} & \text{for } u \geq u_0 \text{ and } \theta_d \leq -0.5 \text{ K;} \\ 0 & \text{otherwise,} \end{cases} \quad (7)$$

where θ_d is the potential temperature deviation from the warm-side sounding. The coefficient C_M is set to $0.8 \times 10^{-4} \text{ s}^{-1}$ for all of the simulations described in the next section. In section 5, various values of C_M are used to investigate the sensitivity of AFVs of NCFRs to variations in the magnitude of horizontal shear. The spatial distribution of M_F varies with time associated with the evolution of cold airflow. It should be mentioned that a forcing representing the Coriolis force's turning action on v momentum is not applied to the u -momentum equation. This is because the inclusion of the Coriolis force without implementing a geostrophically balanced thermodynamic term weakens the cross-frontal circulations (e.g., Fovell 1991), making the simulated cold air boundary ill defined for large C_M . Furthermore, the v -momentum forcing is applied only within the low-level cold airflow. This is because the application of the forcing in the full model domain causes a marked increase of the vertical shear of meridional wind in the warm sector, which also complicates the interpretation of simulation results.

The name of a simulation is created by combining the vertical shear of the cross-front wind with the thermodynamic sounding; for example, U5-S0 refers to the simulation initialized with a $U_S = 5 \text{ m s}^{-1}$ cross-front wind and the S0 sounding.

3. Vertical shear experiment

a. Overview of two-dimensional simulations

In this section, the dependence of the AFV of an NCFR on the vertical shear of the ambient cross-front wind and the stability of the stratification is examined. First, the results of 2D runs are presented to show that the initialization method adopted in this study produces realistic structures of cold fronts.

In each simulation, a cold outflow develops in response to the imposed heat and moisture sinks and a convective-scale updraft forms at its leading edge. Figure 4 shows the time series of the maximum vertical velocity w_{max} and the

To replicate the kinematic structure of the leading edge of a cold front for which a significant shear of alongfront wind is present, a momentum forcing is added to the v -momentum equation. The forcing represents the Coriolis force's turning action on the low-level cold airflow directed toward the leading edge and is given by

frontal width W_F for the simulations initialized with the S0 sounding. Here, W_F is defined as

$$W_F = \frac{V_{\text{max}} - V_{\text{min}}}{(\partial v / \partial x)_{\text{max}}}, \quad (8)$$

where $(\partial v / \partial x)_{\text{max}}$ is the maximum horizontal shear of the alongfront wind, and V_{max} and V_{min} are the maximum and minimum alongfront velocities at the level where $(\partial v / \partial x)_{\text{max}}$ is located, respectively. The time series indicates that the simulated fronts settle into quasi-steady state by $t = 10 \text{ h}$. This is also true for simulations initialized with the S1 and S2 soundings (not shown).

Vertical cross sections around the leading edge for U5-S0 and U20-S0 at $t = 12 \text{ h}$ are shown in Fig. 5. The U5-S0 case produces a highly sloped leading edge of cold air and an updraft that slopes significantly back over the cold air (Fig. 5a). The momentum forcing applied in the cold outflow creates a horizontal shear of v (i.e., vertical vorticity) exceeding $8 \times 10^{-3} \text{ s}^{-1}$ at the leading edge (Fig. 5b). Because the frontal slope from the vertical is large, a significant local vertical shear exists at low levels in the region immediately behind the leading edge of cold air (Fig. 5c; $x \sim 74 \text{ km}$). As the ambient vertical shear increases, the cold air leading edge becomes steeper and the frontal updraft becomes stronger. The U20-S0 case produces an almost upright frontal updraft and a deeper horizontal shear zone compared with those in U5-S0 (Figs. 5d,e). The strong local vertical shear zone behind the leading edge is located at higher levels compared with that in U5-S0 (Fig. 5f). Unlike the U5-S0 case, the local vertical shear is weak in the region of large horizontal shear at low levels.

It has been reported that spurious numerically generated gravity waves are produced in simulations of sloping baroclinic zones due to the inconsistency between the horizontal and vertical resolution (e.g., Pecnick and Keyser 1989; Lindzen and Fox-Rabinovitz 1989; Persson and Warner 1991; Snyder et al. 1993; Jorgensen et al. 2003; Iga et al. 2007). Persson and Warner (1991) showed that significant spurious gravity waves will appear if the

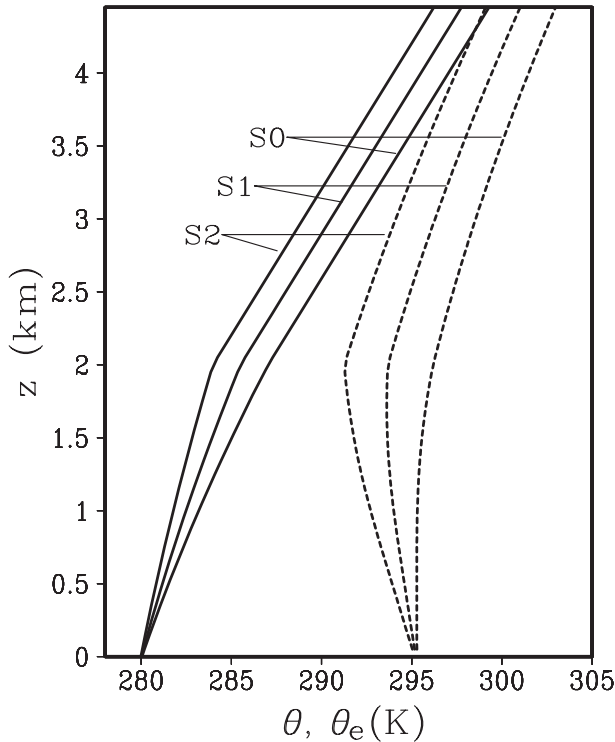


FIG. 2. Vertical profiles of θ (solid line) and θ_e (dashed line) for the S0, S1, and S2 soundings.

sloping frontal structures created by a model are sufficiently strong and sufficiently narrow when measured in grid spaces and the grid aspect ratio $\Delta z/\Delta x$ is larger than the slope of the frontal structures. In some places of the fronts in the present simulations, the grid aspect ratio (0.2 below $z = 1$ km) is larger than the slope of frontal structures, making possible spurious gravity waves. However, no evidence of spurious gravity waves is seen in the present simulations. This is probably because the horizontal resolution adopted in the present study is high enough to resolve the sloped frontal structures. Persson and Warner (1991) also argued that enhanced diffusion will increase the width of the front, thereby decreasing the amplitude of the spurious gravity waves. In the present simulations, parameterized horizontal and vertical diffusions tend to be large along the sloped frontal zone because of the presence of strong wind shear. This may also contribute to the suppression of spurious gravity waves in the present simulations.

Figure 6 depicts key frontal properties as functions of U_S for all of the simulations. For reference, the results of the $U_S = 25 \text{ m s}^{-1}$ trial simulations are also included. For all soundings, the increase in U_S results in an increase in w_{max} until $U_S = 20 \text{ m s}^{-1}$, but further addition of the shear results in a decrease in w_{max} (Fig. 6a). The response of the frontal updraft to the variation in the cross-front

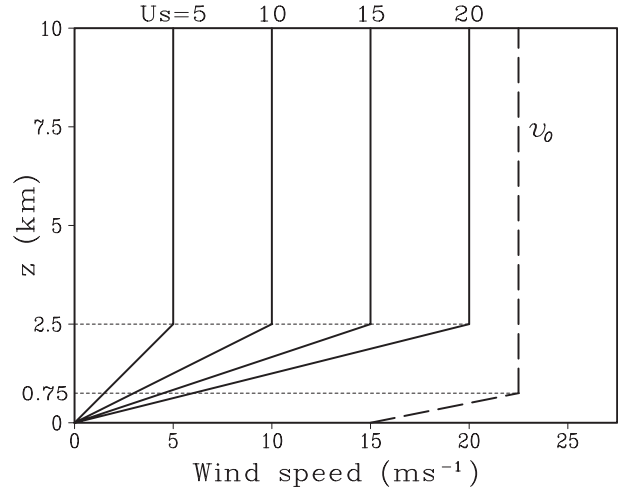


FIG. 3. Initial cross-front (solid line) and alongfront (broken line) wind profiles.

vertical shear is consistent with RKW and Parsons (1992), in that the updraft becomes stronger and more upright with the addition of ambient vertical shear until some optimal values, but further addition of the shear results in

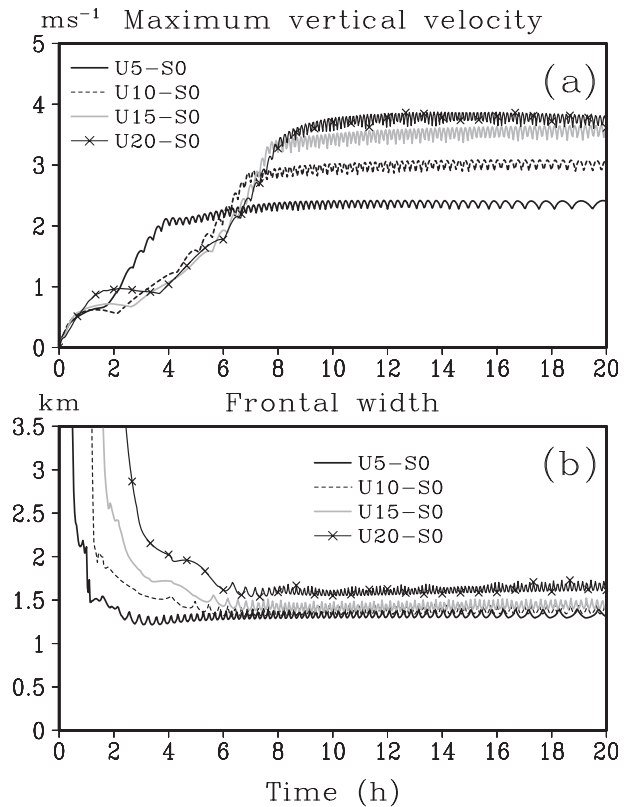


FIG. 4. Time series of (a) w_{max} (m s^{-1}) and (b) W_F (km) for simulations initialized with the S0 sounding.

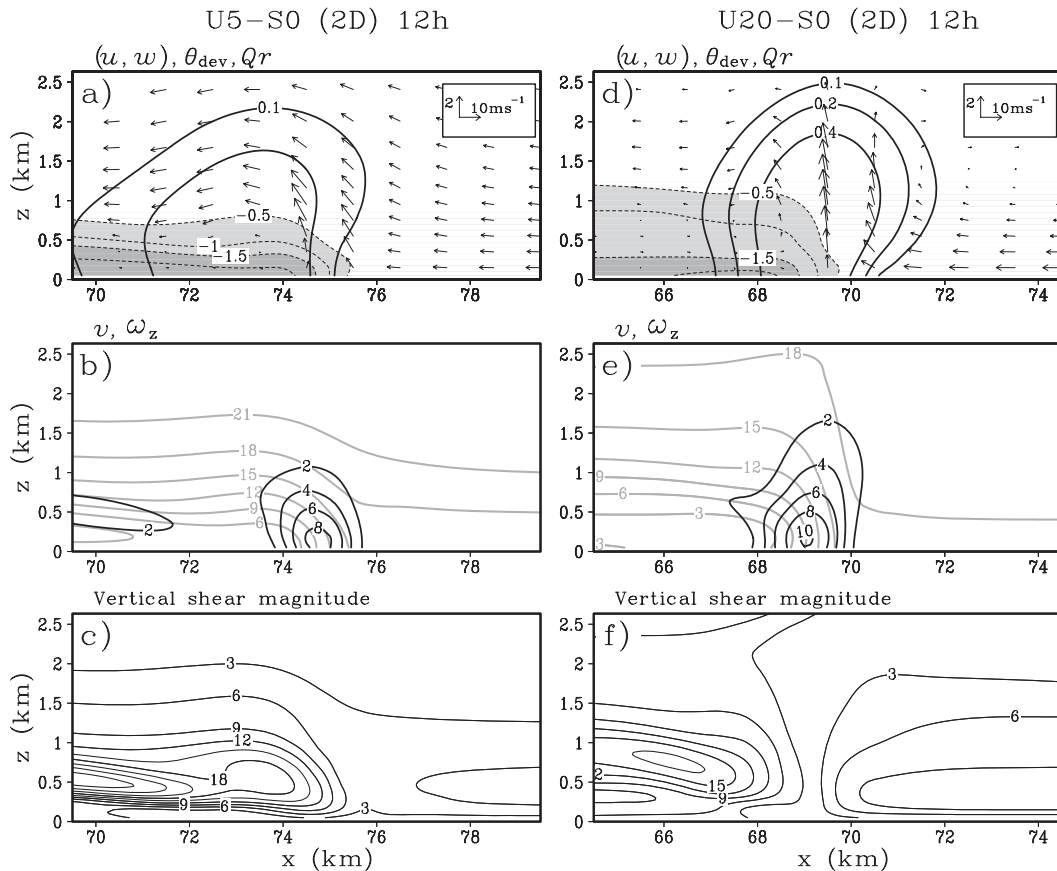


FIG. 5. Two-dimensional frontal fields at $t = 12$ h for (a)–(c) U5-S0 and (d)–(f) U20-S0. (a),(d) Front-relative winds in the plane of the cross section, θ_d (every 0.5 K with zero contour omitted; shaded below -0.5 and -1.5 K), and rainwater mixing ratio (contoured at 0.1, 0.2, and 0.4 g kg^{-1}). (b),(e) Meridional velocity (gray contours, every 3 m s^{-1}) and vertical vorticity (every $2 \times 10^{-3} \text{ s}^{-1}$ with zero contours omitted). (c),(f) Magnitude of vertical shear— $[(\partial u/\partial z)^2 + (\partial v/\partial z)^2]^{1/2}$; every $3 \times 10^{-3} \text{ s}^{-1}$ with zero contours omitted.

the decrease in the updraft strength and downshear tilt of the updraft. The maximum vertical vorticity $\omega_{z\text{max}}$ at the leading edge also increases with the addition of ambient vertical shear until $U_S = 20 \text{ m s}^{-1}$, but its variations with U_S and the stability are less significant compared with that for w_{max} (Fig. 6b). The depth of the horizontal shear zone generally increases with the addition of U_S associated with a steepening of the cold air leading edge (Fig. 6c).

b. Overview of three-dimensional simulations

Using the output of the 2D configuration runs at $t = 12$ h as the meridionally uniform initial conditions, the model is run in its 3D configuration. To introduce three-dimensionality, thermal perturbations were placed along the cold air leading edge. The form of the potential temperature perturbation θ_p inserted into the model initial condition is

$$\theta_p(x, y, z) = \begin{cases} \theta_{py}(y) \sqrt{1 - \left(\frac{x-x_c}{a}\right)^2 - \left(\frac{z}{b}\right)^2} & \text{for } \left(\frac{x-x_c}{a}\right)^2 + \left(\frac{z}{b}\right)^2 \leq 1; \\ 0 & \text{otherwise,} \end{cases} \quad (9)$$

where $\theta_{py}(y)$ represents random perturbations whose magnitude ranges from -0.25 to 0.25 K, x_c is the location of the SCF determined by the maximum in the horizontal gradient of θ , $a = 2$ km, and $b = 1$ km. Unlike

the high-resolution simulations of nonsupercell tornado-genesis by LW97a, lobe and cleft instabilities, which in their simulations were important for triggering HSIs, do not occur along the leading edge in any of the present simulations.

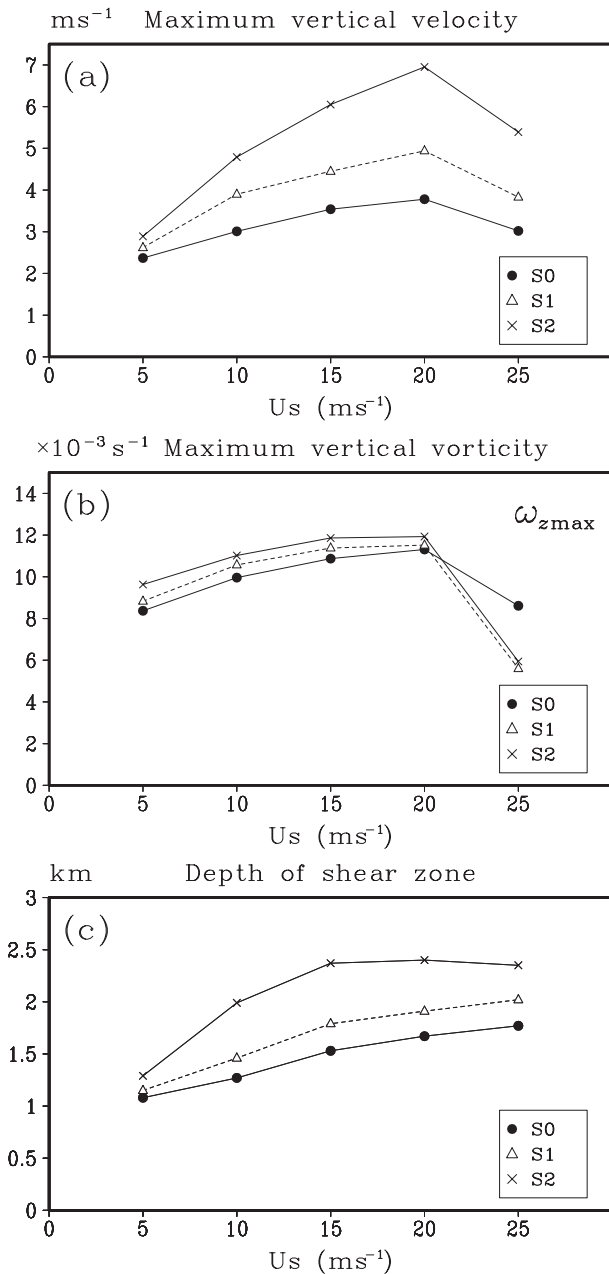


FIG. 6. Plots against U_s of (a) w_{\max} , (b) $\omega_{z\max}$, and (c) the depth of the horizontal shear zone where the vertical vorticity exceeds $2 \times 10^{-3} \text{ s}^{-1}$. Variables shown are averaged over the last 8 h (from 12 to 20 h) of the 2D model integration. The results for the $U_s = 25 \text{ m s}^{-1}$ test simulations are also included.

This is because the leading edge lacks a marked nose structure due to the use of a relatively weak surface friction and a relatively coarse horizontal model resolution.

1) STABLY STRATIFIED CASES

Figure 7 shows the horizontal cross sections of the precipitation intensity normalized by the maximum

precipitation intensity in the domain R_{\max} and the horizontal wind fields around the leading edge at $t = 4$ and 8 h for all of the simulations initialized with the S0 sounding. Hereafter, the simulation time indicated is that from the beginning of the 3D run. It can clearly be seen that the magnitude of the undulation of SCF increases as the vertical shear is increased. As seen from the comparison between $t = 4$ and 8 h, the wavelengths of the AFVs for U5-S0 and U10-S0 change little throughout the simulation period, whereas the AFVs for U15-S0 and U20-S0 show marked upscale growth. The weak undulation of the SCF and weak AFV of precipitation in U5-S0 are consistent with the results of simulation A3D in K07 (see his Fig. 17), for which the prefrontal thermodynamic sounding was also stable to the surface parcel ascent. In U10-S0 and U15-S0, the precipitation is maximized along segments of the SCF that are tilted clockwise from the north, where the perturbed cold front makes largest angle with the prefrontal winds and, therefore, the largest forced convergence occurs. The formation mechanism of PCs for these cases appears to be consistent with the early proposed mechanism whereby HSIs create PCs aligned at a clockwise angle with respect to the synoptic-scale cold front (e.g., Matejka 1980; Hobbs and Persson 1982; Parsons and Hobbs 1983b).

The strongest vertical shear case, U20-S0, produced bow-shaped PCs near the middle of which the precipitation is maximized. As suggested by the relative location of the surface precipitation to the SCF, the tilt of the frontal updraft is upshear at the southern part of the PC, almost upright around the apex of the PC, and downshear at the northern part of the PC. The variation of the updraft tilt along the length of a PC is consistent with those reported in Jorgensen et al. (2003, see their Figs. 14 and 18), though in their case the reflectivity was maximized near the apex or slightly north of the apex of each bow-shaped element. While Jorgensen et al. (2003) suggested that the AFV of the vertical shear of the cross-front ambient flow would account for the variation of updraft tilt, in the present simulation the vertical shear of the prefrontal wind is uniform in the alongfront direction.

Horizontal sections of the vertical vorticity for the regions enclosed by rectangles in Fig. 7 indicate that the near-surface vertical vorticity tends to accumulate at segments of the SCF tilted counterclockwise from the north, where the precipitation intensity is relatively weak (top panels of Fig. 8). This vorticity pattern resembles that found in the early growth stages of shear-instability waves along perturbed vortex sheets associated with parallel shear flows (e.g., Batchelor 1967; Corcos and Sherman 1984), density current interfaces (e.g., LW97a), or the Burgers vortex layer in which the enhancement of vorticity by the spanwise (i.e., along the vorticity direction)

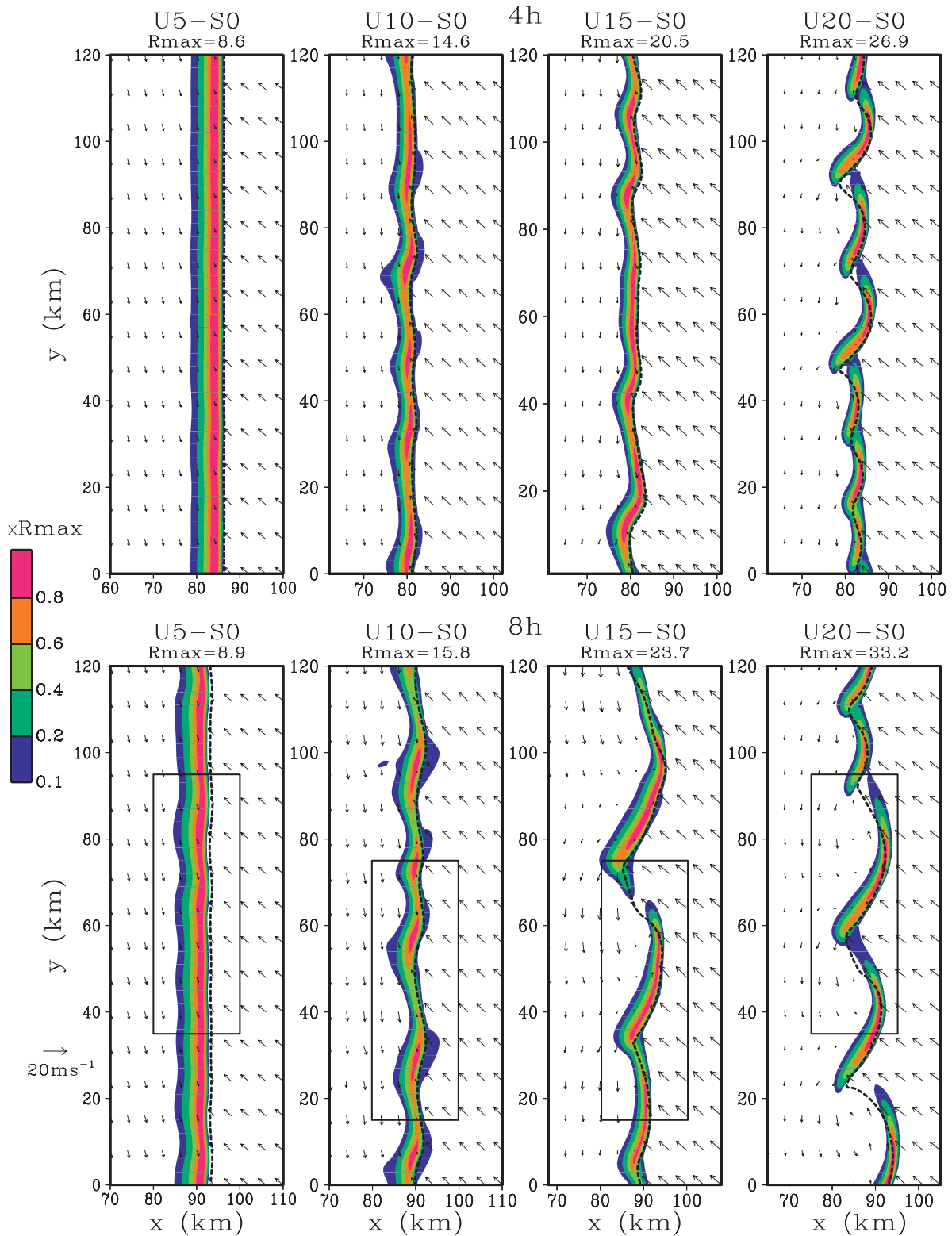


FIG. 7. Horizontal cross sections of the precipitation intensity normalized by R_{\max} (shaded) and the core-relative horizontal winds at the lowest grid level ($z = 50$ m) at (top) 4 and (bottom) 8 h for simulations initialized with the S0 sounding. The thick dashed line in each panel denotes the location of the SCF. Only a $40 \text{ km} \times 120 \text{ km}$ portion of the full domain is shown. R_{\max} (mm h^{-1}) is indicated above each panel. Rectangles indicate the horizontal domains displayed in Fig. 8.

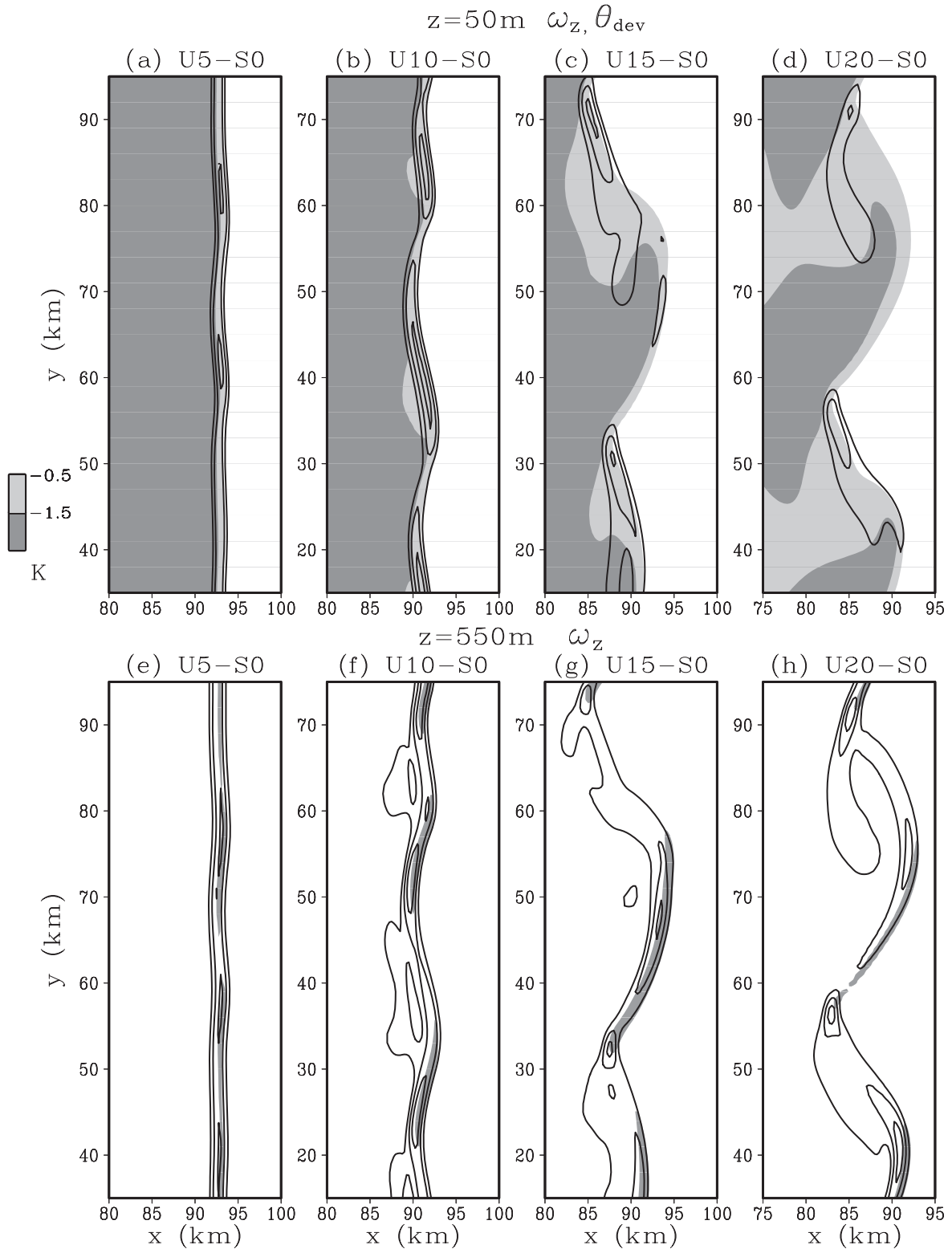


FIG. 8. Horizontal cross sections at $t = 8$ h for the regions enclosed by rectangles in Fig. 7. (a)–(d) ω_z ($3 \times 10^{-3} \text{ s}^{-1}$ contour interval with zero contours omitted) and θ_{dev} (shaded below -0.5 and -1.5 K) at the lowest grid level ($z = 50$ m). (e)–(h) ω_z ($2 \times 10^{-3} \text{ s}^{-1}$ contour interval with zero contours omitted) at $z = 550$ m. Areas of updraft greater than 2 m s^{-1} are shaded in (e)–(h).

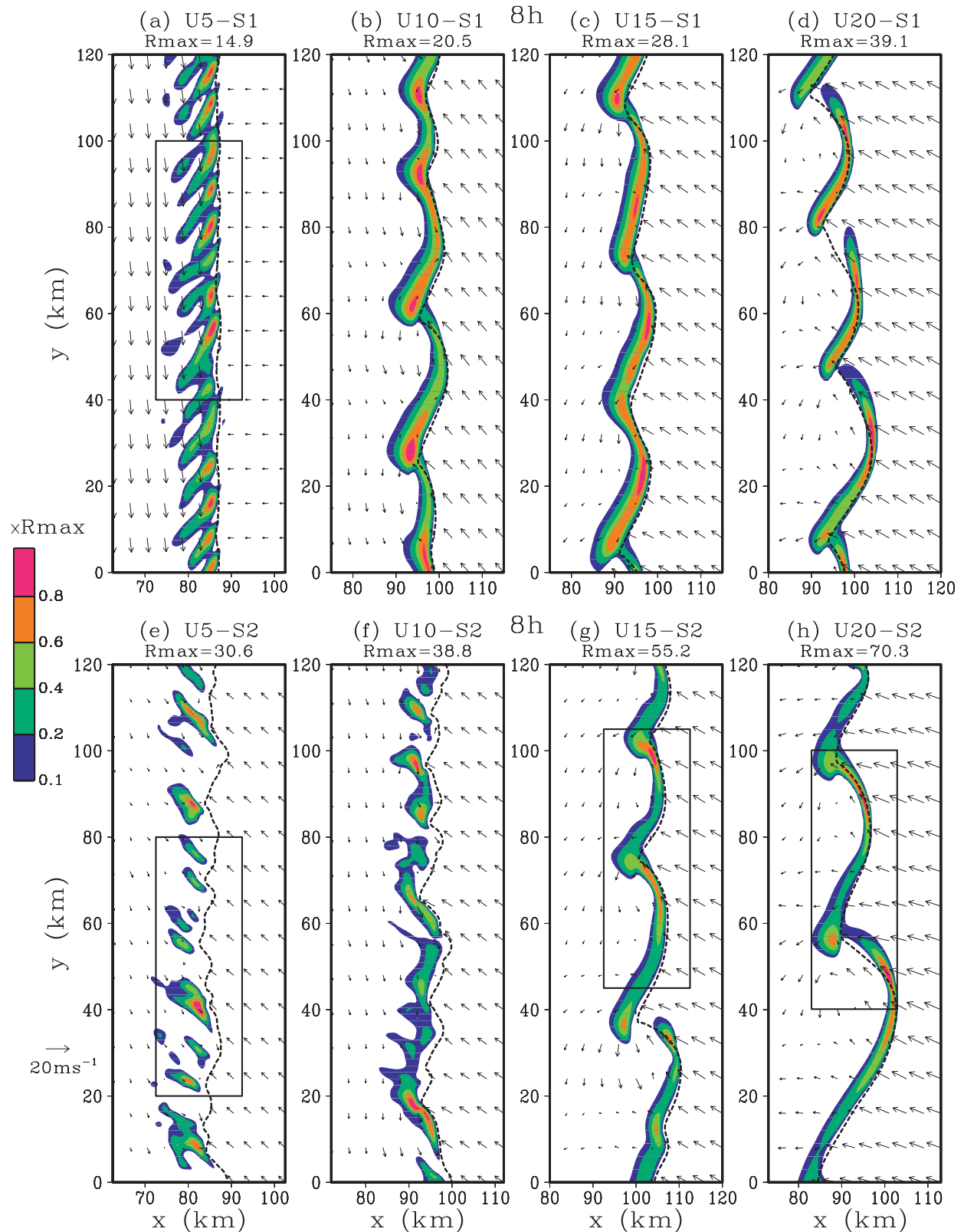


FIG. 9. As in Fig. 7, but for simulations initialized with the (top) S1 and (bottom) S2 soundings at $t = 8$ h. Rectangles indicate the horizontal domains displayed in Fig. 10.

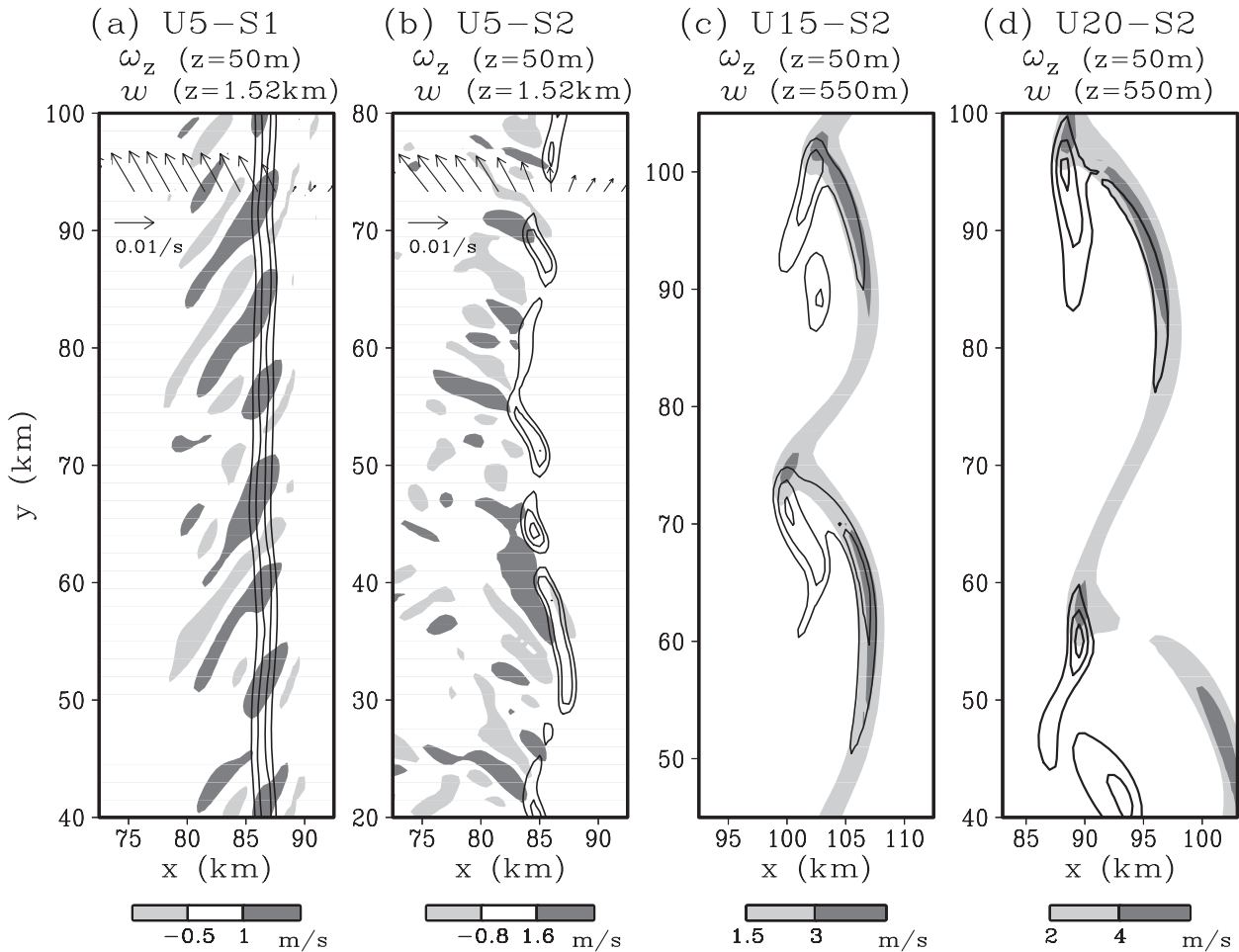


FIG. 10. Horizontal cross sections of ω_z at $z = 50 \text{ m}$ ($3 \times 10^{-3} \text{ s}^{-1}$ interval with zero contours omitted) and w (gray-shade scale at the bottom of each panel) for the regions enclosed by rectangles in Fig. 9 for (a) U5-S1, (b) U5-S2, (c) U15-S2, and (d) U20-S2, showing w fields at (a),(b) $z = 1.52 \text{ km}$ and (c),(d) $z = 550 \text{ m}$. Mean vertical shear of y -averaged horizontal winds between $z = 0.75$ and 2.0 km are also shown by vectors in (a) and (b).

strain is balanced by diffusion (e.g., Lin and Corcos 1984; Neu 1984). Such vortex sheets subsequently show highly nonlinear behavior characterized by vortex sheet roll-up and formation of almost circular vorticity patches. However, the patches of near-surface large vertical vorticity in the present case are highly elongated and remained tilted upshear with respect to the mean alongfront wind. This point will be further discussed later. In U10-S0, U15-S0, and U20-S0 the horizontal gradient of temperature is weak in the region where the precipitation is weak, consistent with the observations by James and Browning (1979), Hobbs and Persson (1982) and Wakimoto and Bosart (2000).

The spatial distributions of the vertical vorticity at $z = 550 \text{ m}$ are rather different from those at $z = 50 \text{ m}$. In the U5-S0 and U10-S0 cases (Figs. 8e,f), maxima in the vertical vorticity are found along the segments of the cold

fronts tilted clockwise from the north, where frontal updrafts are also strong. This suggests that vertical stretching provides an important contribution to vorticity at this level. These vorticity maxima are also associated with the enhanced precipitation along the cold fronts, consistent with the observation by Wakimoto and Bosart (2000; see their Fig. 6). This is also true for the vorticity in the U15-S0 and U20-S0 cases (Figs. 8g,h); however, the vertical vorticity maxima found at the clefts of the cold air in Figs. 8c,d are still evident at this level.

2) UNSTABLE CASES

Figure 9 shows the precipitation intensities at $t = 8 \text{ h}$ for simulations initialized with the S1 and S2 soundings and Fig. 10 shows vertical vorticity at $z = 50 \text{ m}$ and vertical velocity at an indicated level for the regions enclosed by rectangles in Fig. 9. Mean vertical shear of y -averaged

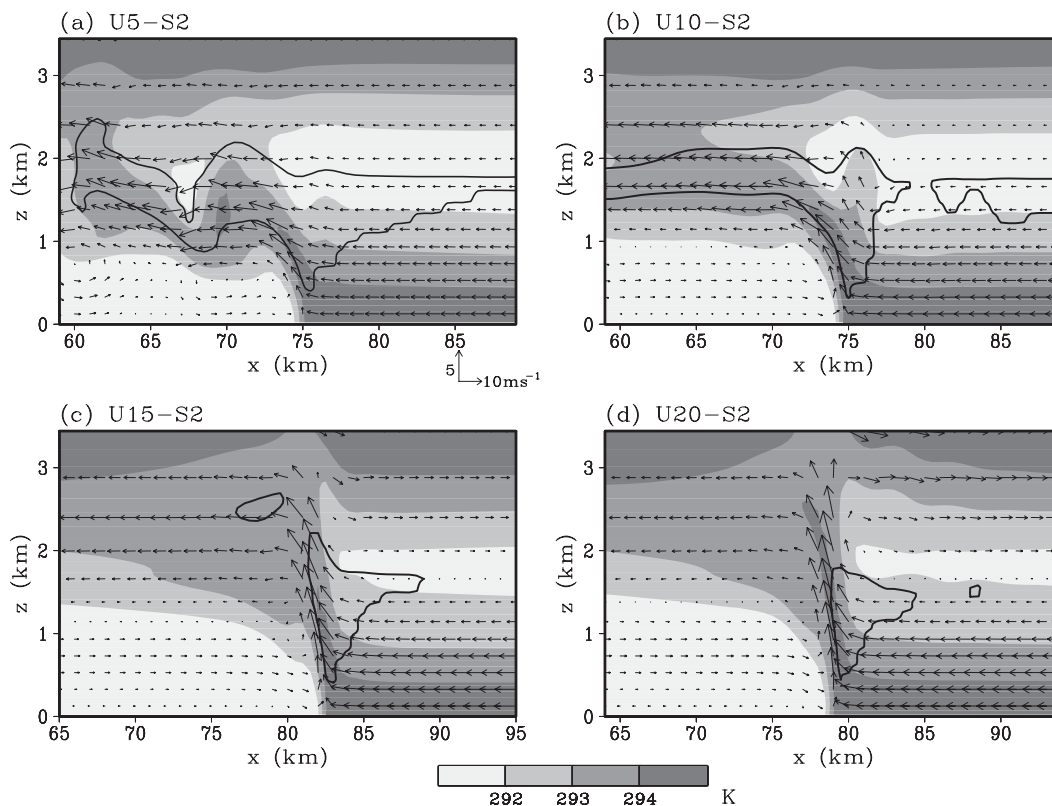


FIG. 11. θ_e (shaded) and front-relative winds in the plane of the cross section at $t = 12$ h of 2D configuration runs for (a) U5-S2, (b) U10-S2, (c) U15-S2, and (d) U20-S2. The solid contour encloses regions where $N_m^2 < 0$.

horizontal winds between $z = 0.75$ and 2.0 km are also shown by vectors for the U5-S1 and U5-S2 cases in Fig. 10. In these cases, velocity perturbations are large in this layer. As in the U5-S0 case, the undulation of the SCF is weak in U5-S1, but the precipitation along the leading edge breaks into regularly spaced PCs oriented clockwise from the north (Fig. 9a). These features are similar to those of the CNTL3D simulation in K07 (his Fig. 10). The dynamical structure of the AFV for U5-S1 shown in Fig. 10a is also similar to that of CNTL3D in K07. The AFV of near-surface vertical vorticity is rather weak, while the vertical velocity field at $z = 1.52$ km (above the frontal surface) exhibits a well-regulated, wavelike structure consisting of an alternating series of upward and downward motions.

Weckwerth and Wakimoto (1992) documented a case in which intersections between a gust front and horizontal vortex lines associated with Kelvin–Helmholtz (K-H) waves with wave crests oriented nearly perpendicular to the gust front produced updraft maxima along the gust front. Similar intersections of horizontal vortex lines and a cold air leading edge were also reported for a nonprecipitating cold front studied by Friedrich et al. (2008). The phase lines of the vertical velocity perturbation for U5-S1

are oriented nearly perpendicular to the direction of the mean vertical shear. However, the wave is different from the simple K-H waves, in that the wave derives most of its energy from both the vertical shear and the buoyancy as shown in the next section.

In the U5-S2 case, PCs are oriented counterclockwise to the cold front and the SCF shows significant undulations (Fig. 9e). The vertical velocity field for this case shows elongated updrafts and downdrafts extending from the leading edge toward the northwest, and phase lines of the vertical velocity perturbations are oriented roughly parallel to the local vertical shear (Fig. 10b). These features are consistent with K07's large CAPE simulations (his section 4), although the irregularity of the AFV is significant in the present case. Thus, the structure of the AFV and its dependence on the stability of the prefrontal environment in the $U_S = 5 \text{ m s}^{-1}$ simulations are generally consistent with K07, despite the differences in the frontal initialization method. The U10-S2 case (Fig. 9f) exhibits qualitatively similar AFVs to those found in U5-S2, although the PCs are less differentiated from each other.

In other cases, the convective-scale features of AFVs noted above are absent and the structures of the AFVs

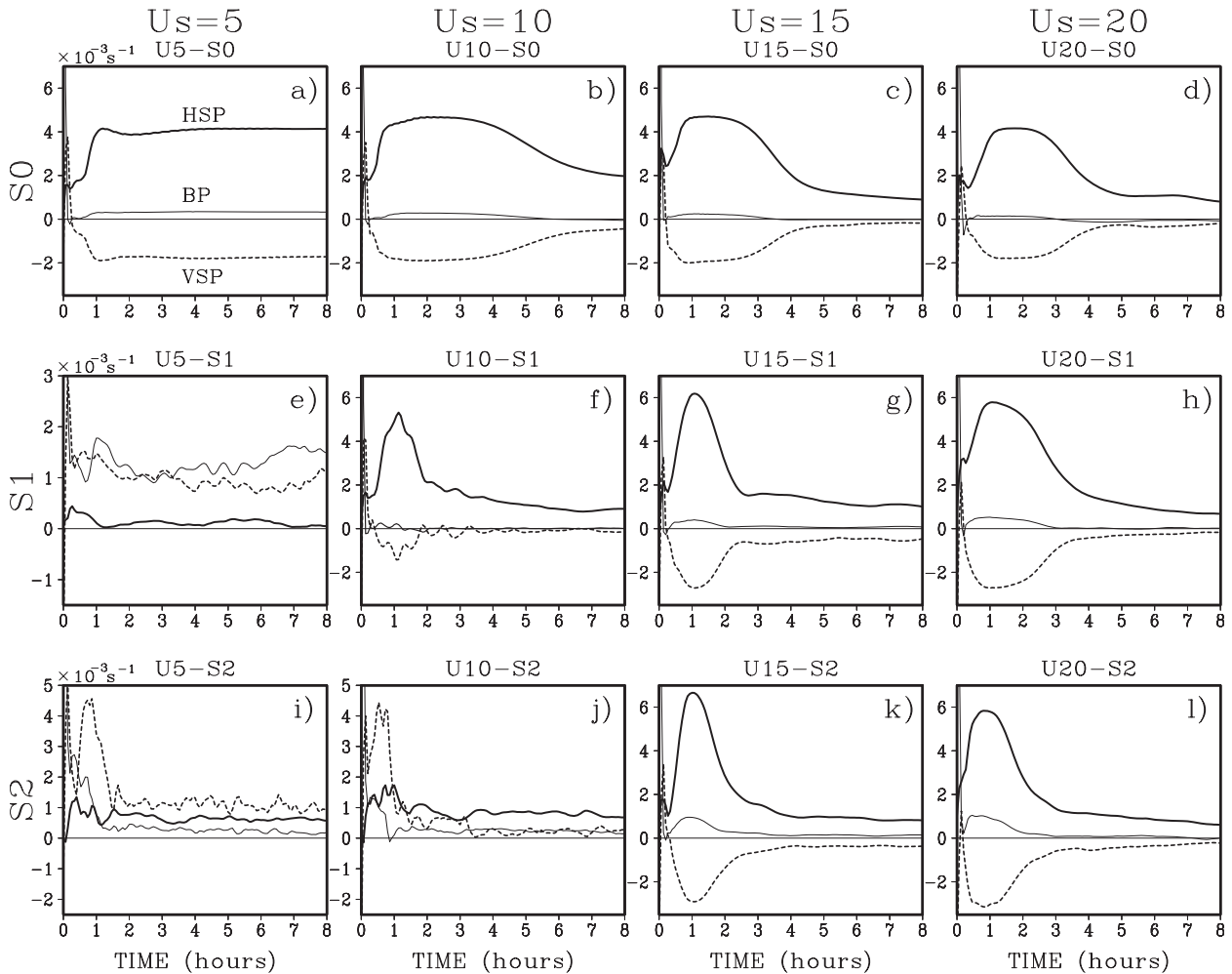


FIG. 12. Time evolutions of the HSP (thick solid), VSP (dashed), and BP (thin solid) terms averaged over the whole calculation domain for each case. Each term is divided by the instantaneous value of the domain-averaged EKE and has a unit of $10^{-3} s^{-1}$.

are basically the same as those found in the corresponding S0 simulations in Fig. 7. However, unlike the S0 sounding cases, the precipitation tends to be maximized north of the apex of each lobe of cold air in the U15-S2 and U20-S2 cases. The PCs for U20-S2 are similar in appearance to those reported by Jorgensen et al. (2003), although in this case precipitation is also maximized in regions immediately behind the clefts of cold air. Comparison of Figs. 8 and 10 for the $U_S = 15$ and $20 m s^{-1}$ cases indicates that the vertical vorticity at $z = 50 m$ is more concentrated near the clefts of cold air in the S2 sounding cases than in the S0 sounding cases. Furthermore, while the maxima in vertical velocity in the S0 sounding cases are found along the segments of the cold front tilted clockwise from the north (Figs. 8g,h), those in the S2 sounding cases are found near the apex or north of the apex of each lobe of cold air (Figs. 10c,d).

Many studies have demonstrated that mesocyclones along air mass boundaries distort the boundaries and produce local maxima of low-level convergence and vertical velocity in their vicinity, which often could be preferred regions to form clouds and/or radar reflectivity cores (e.g., Wilson et al. 1992; Atkins et al. 1995; Lee and Wilhelmson 1997b; Friedrich et al. 2005; Arnott et al. 2006; Murphey et al. 2006; Marquis et al. 2007; Wakimoto and Murphey 2009). Although well-defined vortices with quasi-circular vorticity contours do not develop in the present simulations, it is suggested that in the U15-S2 and U20-S2 cases the concentrated vertical vorticity distorted the horizontal wind field and enhanced the low-level convergence in the vicinity of the vorticity maxima, leading to formation of the precipitation maxima north of the bow apexes.

The qualitative difference of the structure of AFVs between weak and strong vertical shear cases initialized

with unstable soundings can be explained by Fig. 11, which shows the distributions of moist absolutely unstable layers (MAULs; e.g., Bryan and Fritsch 2000; Bryan 2005) and θ_e for the 2D simulations initialized with the S2 sounding. Here, MAULs are identified in the model output where a grid point is saturated and the squared Brunt–Väisälä frequency for saturated air N_m^2 calculated following Durran and Klemp (1982) is less than zero. The dependence of the horizontal and vertical extent of MAULs on the ambient vertical shear is consistent with that noted by Bryan (2005) for numerically simulated squall lines. The U5-S2 and U10-S2 cases, wherein the frontal updrafts are tilted strongly upshear, exhibit horizontally contiguous MAULs above the cold air. In such a situation, the strong local vertical shear above the cold air can align the convective updrafts in the MAUL in the shear direction, as discussed by Bryan et al. (2007). In contrast, MAULs are identified only in narrow regions immediately ahead of the cold air in U15-S2 and U20-S2, wherein the frontal updrafts are more upright. Convective-scale AFVs can hardly develop in such a situation because the residence time of air parcels within the MAUL becomes too short to allow significant convections to develop (e.g., Fuhrer and Schär 2005; Kirshbaum et al. 2007). Though not shown, U5-S1 also exhibits a MAUL above the cold air. However, the horizontal extent of the MAUL is small compared with those in U5-S2 and U10-S2, which probably prevented the formation of convective rolls aligned in the vertical shear direction.

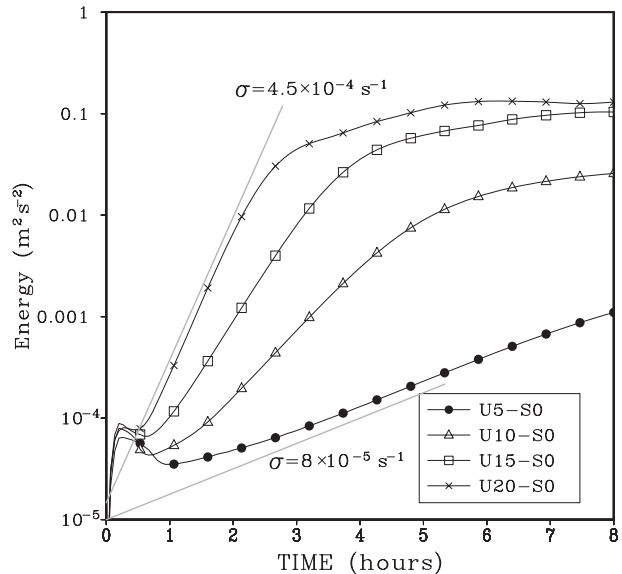


FIG. 13. Time evolutions of the EKE averaged over the whole calculation domain for the simulations initialized with the S0 sounding. For reference, the EKEs for exponentially growing disturbances with constant growth rates of 4.5×10^{-4} and $8 \times 10^{-5} \text{ s}^{-1}$ are indicated by gray straight lines.

c. Energetics

Further insights into the properties of the AFVs of NCFRs can be derived from a consideration of the energetics of the disturbances. Following K07, the equation for the eddy kinetic energy (EKE) budget is written as

$$\begin{aligned} \frac{\partial \bar{K}_e}{\partial t} = & \underbrace{-\overline{v'_i u'} \frac{\partial \bar{v}_i}{\partial x}}_{\text{HSP}} - \underbrace{\overline{v'_i w'} \frac{\partial \bar{v}_i}{\partial z}}_{\text{VSP}} + \underbrace{\overline{B' w'}}_{\text{BP}} - \underbrace{C_p \theta_{v0} \frac{\partial}{\partial x} (\overline{\pi'_1 u'})}_{\text{EFC}} - \underbrace{C_p \theta_{v0} \frac{\partial}{\partial z} (\overline{\pi'_1 w'})}_{\text{EFC}} - \underbrace{\left(\bar{u} \frac{\partial}{\partial x} + \bar{w} \frac{\partial}{\partial z} \right) \bar{K}_e}_{\text{ADV}} \\ & - \underbrace{C_p \theta_{v0} \overline{\pi'_1 \nabla \cdot \mathbf{v}'}}_{\text{RTI}} - \underbrace{\overline{\mathbf{v}' \cdot \nabla K_e}}_{\text{ET}} + \underbrace{\overline{M'_F v'}}_{\text{MF}} - \text{dissipation terms,} \end{aligned} \quad (10)$$

where $i = 1, 2, 3$; $(v_1, v_2, v_3) = (u, v, w)$; and $\bar{K}_e = (\overline{u'^2} + \overline{v'^2} + \overline{w'^2})/2$. The overbar denotes the meridional average, and the prime the deviation from the average. All of the terms except MF (defined below) are described in detail in K07. Among several conversion terms, the terms HSP (horizontal shear production), VSP (vertical shear production), BP (buoyant production), and MF have net contributions to the total EKE increase/decrease. The term MF represents the EKE production due to the correlation between the deviation part of the meridional momentum forcing M'_F and v' . However, MF is two orders of magnitude smaller than HSP and VSP and has little direct influence on the energetics of the AFV.

Time evolutions of the domain-averaged HSP, VSP, and BP terms for each case are shown in Fig. 12. Note that each term has been divided by the domain-averaged EKE to clearly show the relative importance of each term during the early growth stage. The energetics for U5-S1 and U5-S2 cases are qualitatively similar to that for the CNTL3D and large CAPE simulations in K07, respectively (see his Figs. 14a and 21). In U5-S1 (Fig. 12e), the main energy sources are VSP and BP, and HSP is much smaller than these two terms throughout the simulation period. On the other hand, the contribution of HSP is also significant in U5-S2 (Fig. 12i). The time evolution of terms in the early simulation period for U10-S2 (Fig. 12j)

U10-S0 ($t=3\text{h}$)

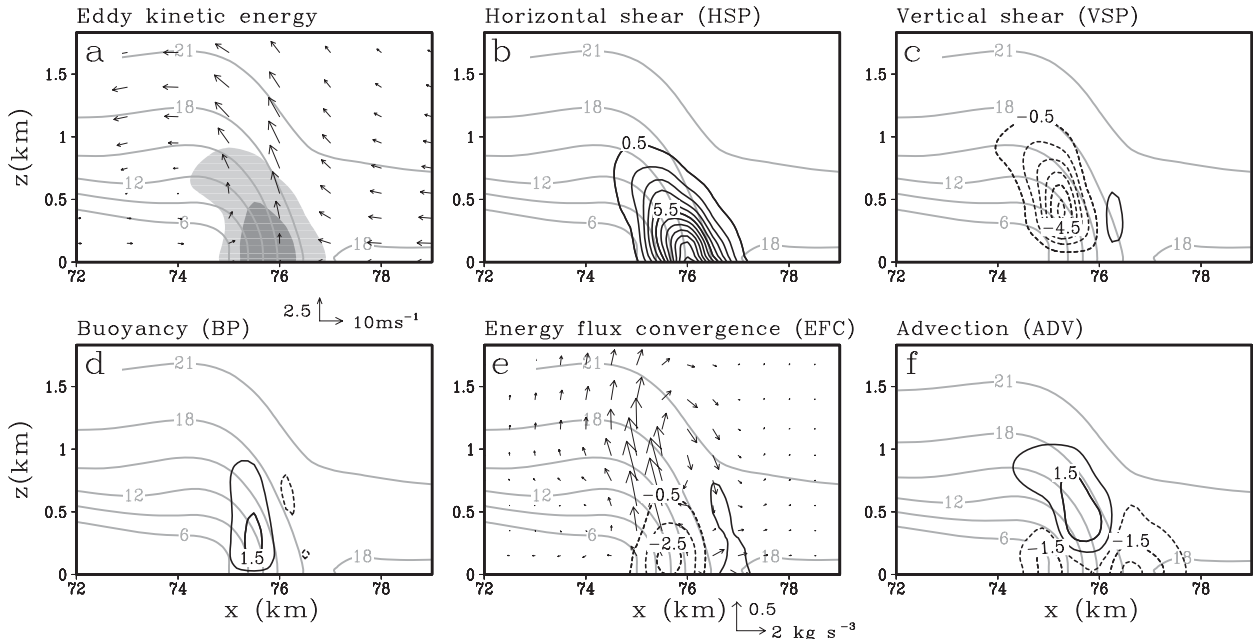


FIG. 14. Spatial distributions of the EKE and energy terms divided by the maximum EKE in the domain for U10-S0 at $t = 3$ h: (a) normalized EKE, (b) HSP, (c) VSP, (d) BP, (e) EFC and energy flux vectors ($C_p \theta_{v0} \overline{\pi_1' u'}$, $C_p \theta_{v0} \overline{\pi_1' w'}$), and (f) ADV. The normalized EKE is shaded at 0.2 and 0.6 in (a). The contour interval for energy terms is $1 \times 10^{-3} \text{ s}^{-1}$ starting at $\pm 0.5 \times 10^{-3} \text{ s}^{-1}$. Also, \bar{v} (3 m s^{-1} contour interval) is superimposed on each panel as gray contours.

is similar to that in U5-S2, but the term HSP becomes dominant beyond $t = 3$ h.

In all other cases, the main conversion is due to HSP, whereas VSP acts as a significant sink term. This indicates that the disturbance gains energy from the mean horizontal shear flow through horizontal Reynolds stresses, whereas simultaneously generated vertical Reynolds stresses feed the disturbance's energy into the mean vertical shear flow. The magnitude of BP is small compared with that for HSP and VSP.

The time evolutions of the domain-averaged EKE for simulations initialized with the S0 sounding are displayed in Fig. 13 using a log-scaled ordinate. After a short period of initial adjustment, the EKE for each case grows exponentially at an almost constant growth rate (linear in Fig. 13). The comparison between Figs. 12 and 13 indicates that the magnitude of each energy term is relatively large in the exponential growth stage of EKE. All of the hydrodynamic fields (i.e., u' , v' , w' , and θ') for each case also grow at a common constant rate in that stage (not shown), indicating that the instability is essentially linear. Hereafter, AFVs for which the main energy source is HSP is referred to as the HSI-type AFVs or the HSI waves, although the instability characteristics are rather different from those for parallel shear flows, as shown later. It is evident in Fig. 13 that the growth rates and the

amplitudes of the HSI waves decrease markedly with decreasing ambient vertical shear. The differences in growth rates between the cases are much larger than those expected from the differences in the vertical vorticity shown in Fig. 6b.

The spatial distributions of the EKE and energy terms for U10-S0 in the linear instability phase ($t = 3$ h) are displayed in Fig. 14. The EKE is concentrated at the cold air leading edge (Fig. 14a), where the generation of EKE by HSP is also large due to the presence of strong horizontal shear (Fig. 14b). The depletion of EKE by VSP occurs in the region immediately behind the leading edge because the local vertical shears of both the cross-front and alongfront winds are large there (Fig. 14c). A small EKE generation by BP occurs at the leading edge (Fig. 14d), where the undulation of shear zone results in the generation of eddy potential energy that will be converted into EKE. Although energy flux convergence (EFC) and advection of EKE (ADV) do not have net contributions to the volume-averaged EKE, these terms act to transport the EKE upward from the region of large EKE generation by HSP (Figs. 14e,f). The distributions of energy terms for other HSI-type cases are basically the same as those in Fig. 14. However, as shown in Fig. 15a, the removal of EKE by VSP behind the leading edge in the U5-S0 case is somewhat larger and

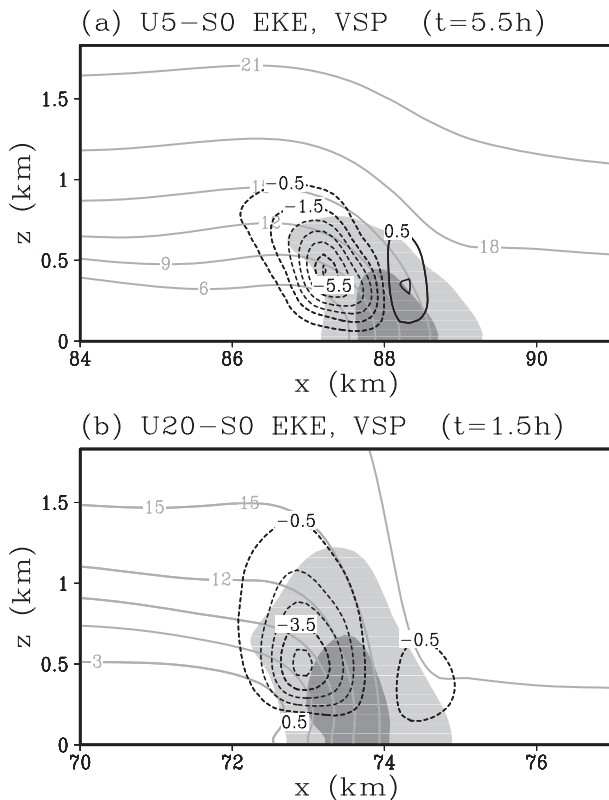


FIG. 15. Spatial distributions of the EKE and the VSP term divided by the maximum EKE in the domain for (a) U5-S0 at $t = 5.5$ h and (b) U20-S0 at $t = 1.5$ h. The normalized EKE is shaded at 0.2 and 0.6. The contour interval for VSP is $1 \times 10^{-3} \text{ s}^{-1}$ starting at $\pm 0.5 \times 10^{-3} \text{ s}^{-1}$. Also, \bar{v} (3 m s^{-1} contour interval) is superimposed on each panel as gray contours.

occurs at lower levels because the frontal slope from the vertical and the local vertical shear increase as the ambient vertical shear is reduced. In contrast, in the U20-S0 case, the removal of EKE by VSP behind the leading edge is smaller and is located at higher levels (Fig. 15b). Note also that a negative VSP region appears immediately ahead of the leading edge because of the presence of strong positive vertical shear of cross-front wind there (see Fig. 5f).

It should be mentioned that the specific vertical shear magnitude above which HSI-type AFVs occur in unstable sounding cases depends strongly on the temperature difference across the cold front because the structure of the uplifting of prefrontal unstable air depends strongly on the balance between the strength of cold air and the ambient vertical shear (e.g., RKW). However, the structural similarity of HSI-type AFVs with many previous observations and the strongly sheared environments typical of cold fronts (e.g., Houze et al. 1976) suggests that an HSI-type disturbance will be a more common type of AFV of NCFRs than those reported in K07. Thus, remaining discussions will be focused on HSI-type AFVs.

4. Mechanisms of HSI wave suppression

It is shown in the previous section that the growth rates and amplitudes of HSI-type AFVs decrease as the vertical shear of the ambient cross-front wind is reduced. This tendency is qualitatively consistent with the results of numerical simulations of nonsupercell tornadogenesis of LW97a (their Figs. 16 and 17). LW97a attributed the delay or the absence of mesocyclone development in their negative vertical shear or unsheared cases to a lack of outflow nose structure, which is conducive to the lobe and cleft instabilities that trigger HSIs. However, the simulated leading edge lacks nose structure and therefore is free from lobe and cleft instabilities in all of the simulations presented herein. Furthermore, the difference in the growth rates of HSI waves as noted in Fig. 13 cannot be explained by the difference in the magnitude of initial perturbations. In this section, an explanation is offered concerning the significant vertical shear dependency of the HSI wave growth along NCFRs.

The instability of parallel shear flows is often interpreted in terms of the synergetic interaction between two vorticity edge waves that propagate in opposing directions on oppositely signed vorticity gradients (e.g., Bretherton 1966; Hoskins et al. 1985, Fig. 18; Bishop and Thorpe 1994, Fig. 1; Heifetz et al. 1999). The edge waves interact because the vorticity anomalies of one edge wave induce cross-stream velocity at the location of the other wave, and their interaction can result in phase-locking and mutual growth. The concept of edge wave interaction helps explain the significant dependence of HSI wave growth on ambient vertical shear.

Figure 15 suggests that a low-level wave on the western edge of the shear zone is strongly damped by VSP when the ambient vertical shear of cross-front wind is weak. Although a wave on the eastern edge of the shear zone is not directly damped by VSP in weak ambient vertical shear cases, the mutual amplification of low-level edge waves will be strongly inhibited in such a situation.

Because local vertical shear can be related to horizontal vorticity, the mechanisms of HSI wave suppression can also be understood from the perspective of vorticity dynamics with the aid of the concept of edge wave interaction. The vertical vorticity tendency equation for a Boussinesq inviscid fluid can be written as

$$\frac{\partial \omega_z}{\partial t} = \underbrace{-u \frac{\partial \omega_z}{\partial x}}_{\text{ADV}_x} - \underbrace{v \frac{\partial \omega_z}{\partial y}}_{\text{ADV}_y} - \underbrace{w \frac{\partial \omega_z}{\partial z}}_{\text{ADV}_z} + \underbrace{\omega_x \frac{\partial w}{\partial x}}_{\text{TILT}_x} + \underbrace{\omega_y \frac{\partial w}{\partial y}}_{\text{TILT}_y} + \underbrace{\omega_z \frac{\partial w}{\partial z}}_{\text{STR}}. \quad (11)$$

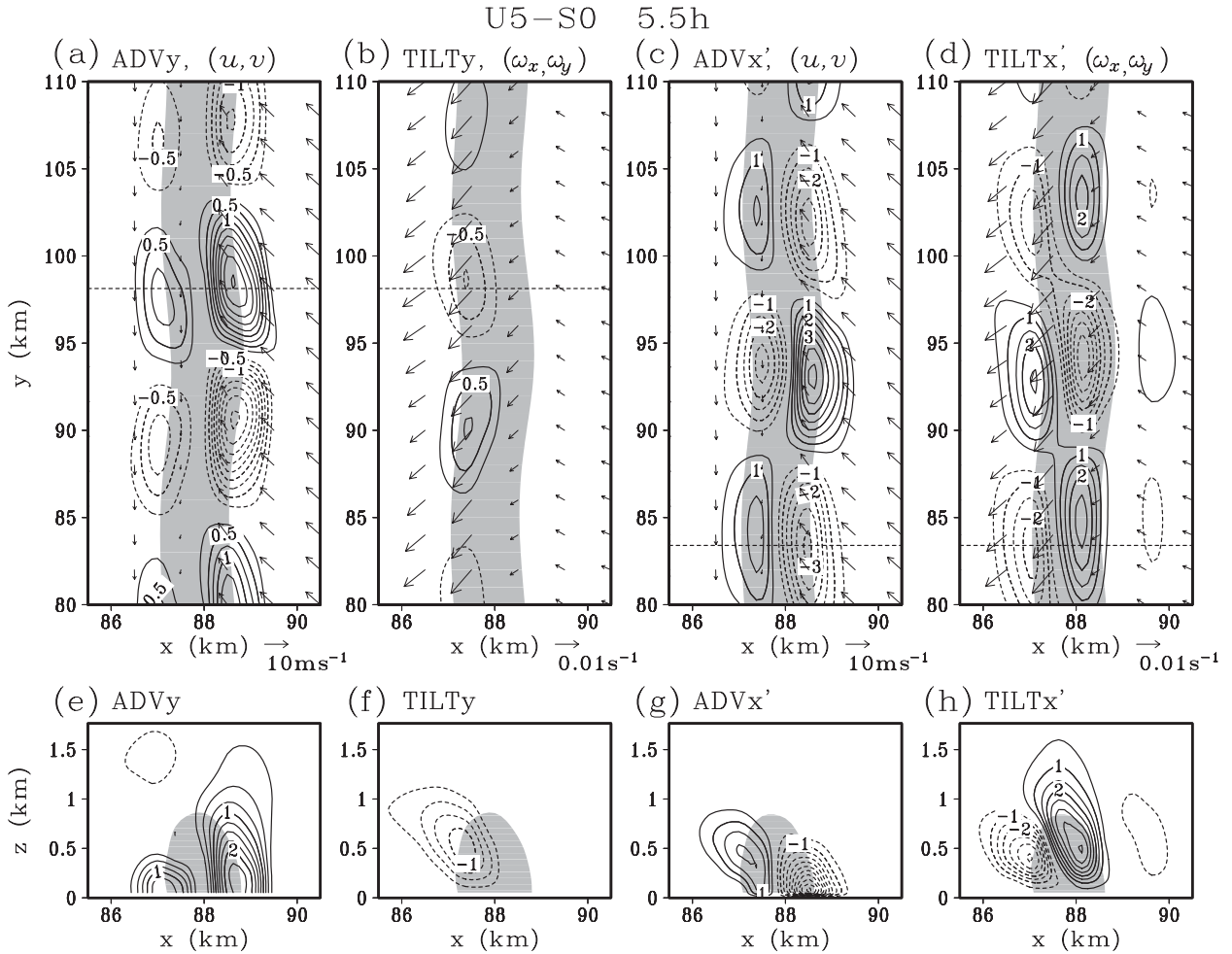


FIG. 16. Spatial distributions of the vorticity tendency terms for U5-S0 at $t = 5.5$ h: (a) ADV_y and core-related horizontal wind vectors, (b) $TILT_y$ and horizontal vorticity vectors (ω_x, ω_y) , (c) ADV_x' and core-related horizontal wind vectors, (d) $TILT_x'$ and horizontal vorticity vectors (ω_x, ω_y) , and (e)–(h) vertical sections along the dashed lines in (a)–(d), respectively. Variables shown are averaged between $z = 50$ and 450 m in (a)–(d). Contour intervals are $0.25 \times 10^{-7} \text{ s}^{-2}$ for ADV_y and $TILT_y$ and $0.5 \times 10^{-7} \text{ s}^{-2}$ for ADV_x' and $TILT_x'$ with zero contours omitted. The shaded area in each panel represents the region where ω_z exceeds $3 \times 10^{-3} \text{ s}^{-1}$. The zonal scale is exaggerated by 2.7 times in (a)–(d) to show the spatial relationship between the tendency terms and the vertical vorticity clearly.

The terms ADV_x , ADV_y , and ADV_z represent the zonal, meridional, and vertical advection of vertical vorticity ω_z , respectively. The terms $TILT_x$, $TILT_y$, and STR represent the tilting of x component of vorticity ω_x , the tilting of y component of vorticity ω_y , and the stretching of vertical vorticity, respectively. The growth of HSI along a shear zone occurs through the differential horizontal advection of ω_z by ADV_y and ADV_x , whereas $TILT_y$ and $TILT_x$ oppose this growth, as shown below.

Figure 16 shows the spatial distributions of ADV_y and $TILT_y$ as well as the deviations of ADV_x and $TILT_x$ from their y averages (ADV_x' and $TILT_x'$) for U5-S0 at $t = 5.5$ h. Here, ADV_x' and $TILT_x'$ are shown because ADV_x and $TILT_x$ are almost uniform in the y direction when the amplitude of an HSI wave is small. In the horizontal

sections, averages over the depth between $z = 50$ and 450 m are shown because the meridional advection of the vertical vorticity on the western edge of the shear zone is concentrated in that layer. The term ADV_y (Figs. 16a,e) acts to accumulate ω_z on both edges of the segments of perturbed shear zone rotated counterclockwise from the north ($y \sim 98$ km). The accumulation of ω_z creates a circulation tendency that further enhances the undulation of the shear zone. This effect is represented by ADV_x' (Figs. 16c,g), which shows positive values on the western (eastern) edges of the segments of the shear zone that are displaced westward (eastward) from the mean locations of the vorticity edges. The growth of the vertical vorticity perturbation through the differential horizontal advection is consistent with the qualitative explanation of shear

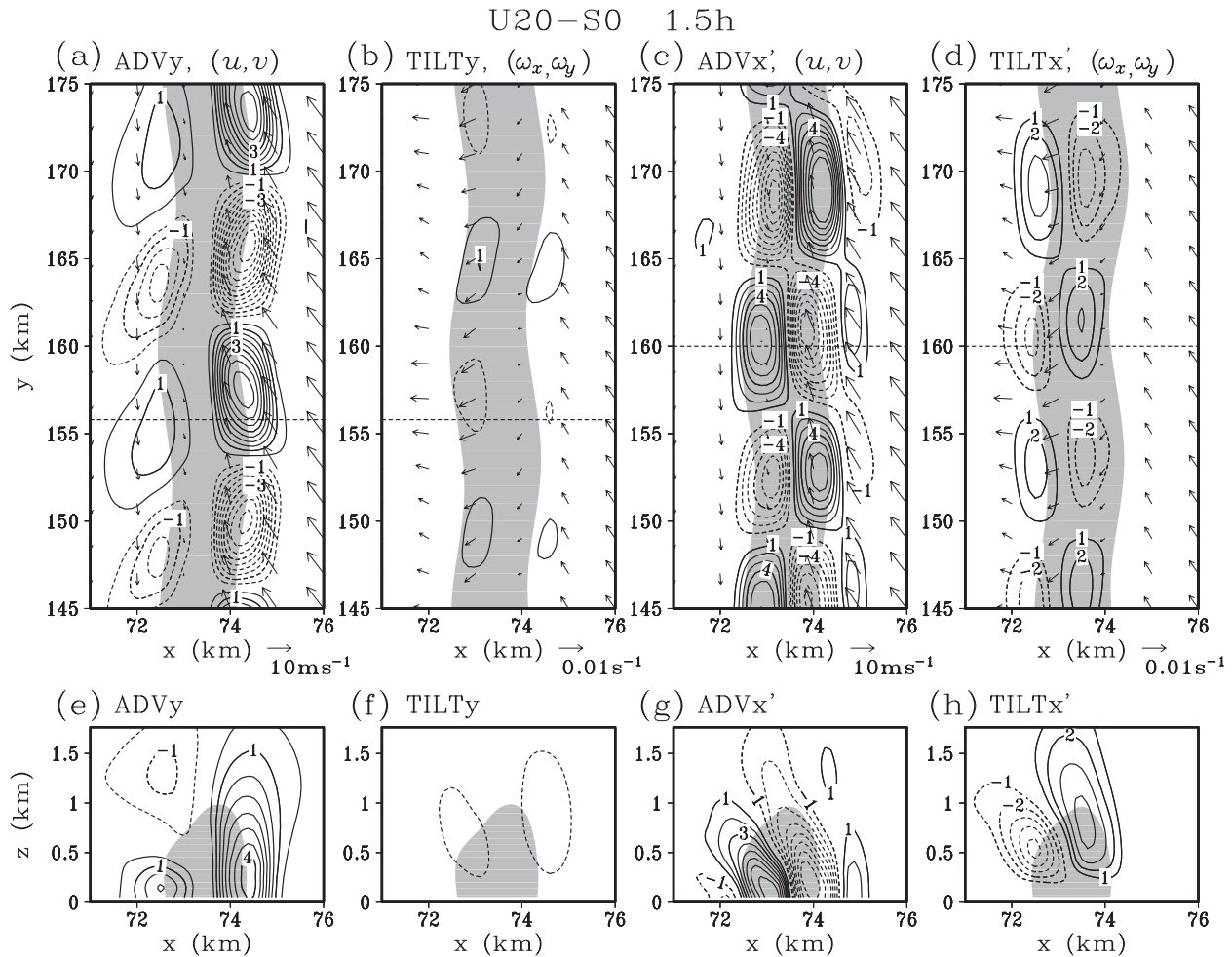


FIG. 17. As in Fig. 16, but for U20-S0 at $t = 1.5$ h. Contour intervals are $0.5 \times 10^{-7} \text{ s}^{-2}$ for ADV_y and $TILT_y$ and $1.0 \times 10^{-7} \text{ s}^{-2}$ for ADV_x' and $TILT_x'$ with zero contours omitted. The shaded area in each panel represents the region where ω_z exceeds $4 \times 10^{-3} \text{ s}^{-1}$.

instability by Batchelor (1967). Because ω_y is negative on the western side of shear zone, $TILT_y$ creates a negative (positive) vorticity tendency along the western edges of the segments of shear zone that are rotated counterclockwise (clockwise) from the north, where the y gradient of w is positive (negative) (Figs. 16b,f). In this case, ADV_y on the western edge of the shear zone is almost completely offset by $TILT_y$ because ω_y on the western side of the shear zone is large. On the other hand, $TILT_x'$ creates a negative (positive) vorticity tendency on the western edges of the segments of the shear zone that are displaced westward (eastward). The values of $TILT_x'$ are negatively correlated and almost in balance with those of ADV_x' on the western edge of the shear zone (Figs. 16d,h). Thus, the growth of the western edge wave and, therefore, the mutual amplification of the vorticity edge waves are strongly suppressed in this case.

For comparison, Fig. 17 shows the distributions of the same terms for the U20-S0 case at $t = 1.5$ h, when the

wave amplitude is almost the same as that in Fig. 16. The spatial distribution of each term on the western edge of the shear zone is qualitatively the same as in Fig. 16. However, ADV_y and ADV_x' on the western edge of the shear zone are only partially offset by $TILT_y$ and $TILT_x'$, respectively, because the magnitudes of ω_x and ω_y in that region are considerably smaller than those in U5-S0. Thus, the mutual amplification of the vorticity edge waves is less inhibited than in U5-S0.

Although the local vertical shear of alongfront wind $\partial\bar{v}/\partial z$ (or ω_x) decreases with decreasing horizontal shear, the local vertical shear of cross-front wind $\partial\bar{u}/\partial z$ (or ω_y) is almost independent of the horizontal shear strength. Thus, a critical value of horizontal shear may exist below which the growth of HSI waves is completely suppressed by the effects of the local vertical shear (or horizontal vorticity), as shown in the next section. Although the suppression mechanism of HSI waves along NCFRs is addressed here, the discussion above may also help explain why lower

tropospheric convergence lines with horizontal shear do not always exhibit significant wave patterns or accompany vortical disturbances that result from HSIs.

5. Horizontal shear experiments

a. Results

LW97a and Lee and Wilhelmson (2000) showed that strength of across-front horizontal shear plays a controlling role in the upscale progression of misocyclones along outflow boundaries. Since the horizontal shear across the cold front also varies from case to case, it is of interest to investigate the sensitivity of the AFVs of NCFRs to variation in horizontal shear strength. For this purpose, simulations presented in the previous sections are repeated for various values of C_M ranging from 0.2×10^{-4} to $1.2 \times 10^{-4} \text{ s}^{-1}$. Although the horizontal shears in the $C_M = 0.2 \times 10^{-4}$ and $0.4 \times 10^{-4} \text{ s}^{-1}$ cases are considerably weaker compared with those of typical cold fronts, these cases are run to demonstrate clearly the dependence of AFV on horizontal shear. On the other hand, test simulations utilizing C_M values greater than $1.2 \times 10^{-4} \text{ s}^{-1}$ indicated that short-wavelength Kelvin–Helmholtz waves develop between the warm and cold air masses because of the enhancement of the local vertical shear, which strongly masks the HSI-type AFVs of interest. Thus, the results for such simulations are not presented here. This parameter study reveals a distinct relationship between the initial wavelength of HSI and the horizontal shear strength. It should be mentioned that in LW97a’s simulations the initial wavelengths of HSIs were determined largely by the scale of lobe and cleft gravitational instabilities, which were triggered by relatively strong thermal perturbations initially distributed along the outflow leading edges.

Figure 18 shows profiles of v across the leading edge for 2D-configuration runs of U10-S0 using various C_M values. The maximum horizontal shear and Reynolds number Re are also indicated. Here, Re is defined as $Re = (V_{\max} - V_{\min})W_F/(2K_m)$, where K_m is the parameterized horizontal eddy-mixing coefficient at the location of maximum horizontal shear. Although the increase of C_M from 0.2×10^{-4} to $1.2 \times 10^{-4} \text{ s}^{-1}$ entails the increase of K_m from about 120 to $200 \text{ m}^2 \text{ s}^{-1}$ (not shown), the qualitative profiles of v and the 2D structures of the cold front remain virtually unchanged.

Figure 19 shows the vertical vorticity field in the exponential growth stage of the EKE, whereas Fig. 20 shows the precipitation intensity at $t = 8 \text{ h}$ for U10-S0 simulations using various C_M values. The growth of HSI waves is completely absent in the simulation using $C_M = 0.2 \times 10^{-4} \text{ s}^{-1}$. This is also true for U5-S0 simulations using

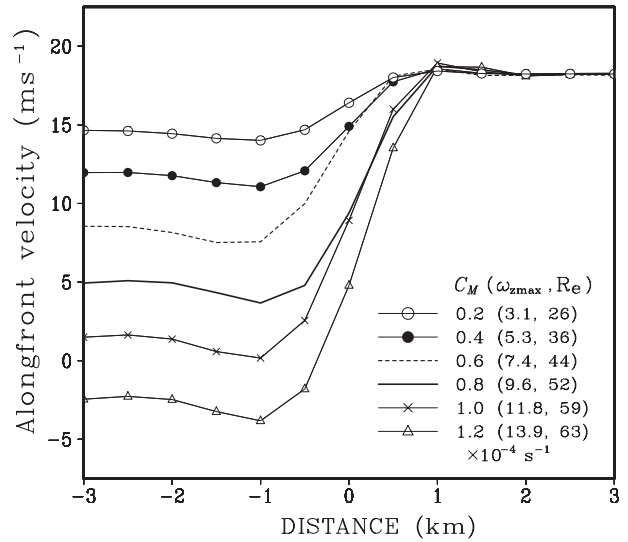


FIG. 18. Horizontal profiles of v at $z = 0.15 \text{ km}$ and $t = 12 \text{ h}$ for the U10-S0 horizontal shear experiments. Re and $\omega_{z\max}$ (10^{-3} s^{-1}) are indicated in the parentheses. The origin along the abscissa represents the location of $\omega_{z\max}$.

$C_M = 0.2 \times 10^{-4}$ and $0.4 \times 10^{-4} \text{ s}^{-1}$ (not shown), suggesting that the critical value of horizontal shear required for HSIs increases as U_S is reduced. It is evident in Fig. 19 that the initial wavelength of AFV increases with increasing horizontal shear, despite the fact that the widths of the horizontal shear zones differ little between the simulations. In this and U5-S0 cases, marked upscale growths of the HSI-type AFVs are absent regardless of the horizontal shear strength; thus, the wavelength of the AFV of precipitation at $t = 8 \text{ h}$ for each case is almost the same as that in the early growth stage of the HSI wave (Fig. 20). The initial wavelength of AFV also increases with increasing horizontal shear for the $U_S = 15$ and 20 m s^{-1} simulations. In these cases, however, the upscale growths of AFVs beyond the exponential growth stage of the HSI waves tend to be enhanced as the horizontal shear is increased, consistent with the results of LW97a and Lee and Wilhelmson (2000) (not shown).

The statistics of the horizontal shear experiments are presented in Fig. 21, which plots the ratio of the mean initial wavelength of AFV λ to the effective width of horizontal shear zone W_E as a function of the horizontal shear for various vertical shear simulations. Here, λ is calculated by dividing L_y by the total number of local vorticity maxima, and W_E is defined as the average of W_F at $t = 0 \text{ h}$ over a depth for which the horizontal average of the HSP in the subsequent exponential growth stage of the EKE exceeds 20% of its maximum value. The horizontal shear in Fig. 21 is the average of maximum horizontal shear over this depth. For all of the cases initialized

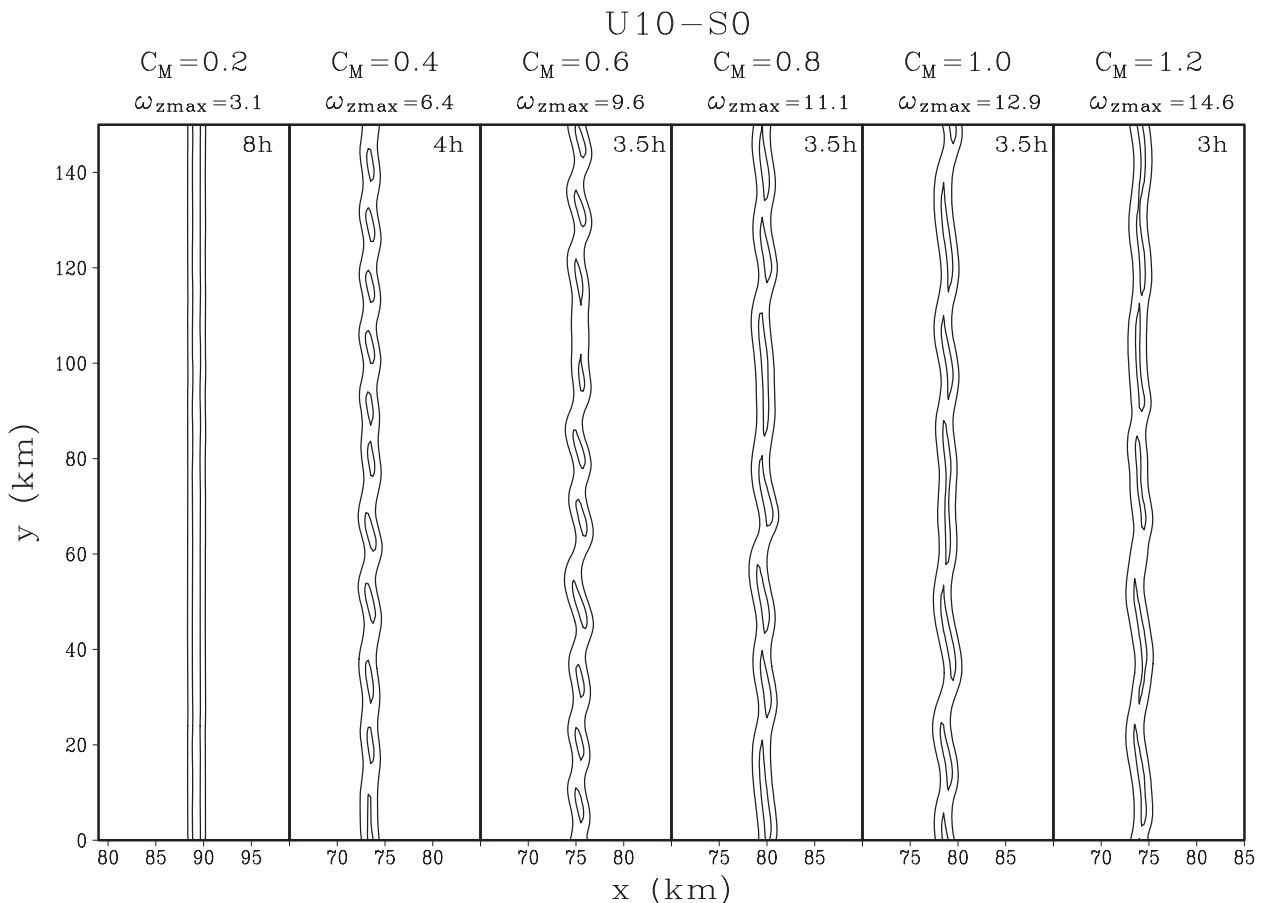


FIG. 19. Horizontal cross sections at $z = 50$ m showing the distributions of ω_z during the exponential growth stage of the EKE for the U10-S0 horizontal shear experiments. The vorticity at $t = 8$ h is shown for the simulation using $C_M = 0.2 \times 10^{-4} \text{ s}^{-1}$, wherein the growth of HSI waves is completely absent. The contours of ω_z are at 20% and 80% of ω_{zmax} in the horizontal sections. The values of C_M (10^{-4} s^{-1}) and ω_{zmax} (10^{-3} s^{-1}) are indicated above each panel. The zonal scale is exaggerated 2 times to clearly show the AFV of ω_z . Only a $20 \text{ km} \times 150 \text{ km}$ portion of the full domain is shown.

with the stable S0 sounding (Fig. 21a), a stronger horizontal shear leads to a larger λ/W_E , except in the weak horizontal shear range where a slight decrease of λ/W_E with increasing horizontal shear is observed in U15-S0 and U20-S0 cases. A similar decreasing tendency for λ/W_E with increasing horizontal shear is observed in unstable sounding cases (Fig. 21b) for a wider horizontal shear range (less than $\sim 6 \times 10^{-3} \text{ s}^{-1}$) compared with the stable sounding cases, but a similar increase of λ/W_E with increasing horizontal shear occurs above that shear range as for the stable sounding cases. It should be mentioned here that the basic horizontal-shear dependency described above was also observed in experiments utilizing a constant K_m .

Numerical analyses of shear instabilities for viscid parallel flows by Betchov and Szewczyk (1963) indicate that the most unstable wavelength decreases with increasing Re if the Re is smaller than approximately 40–50.

Above this Re, the instability becomes essentially insensitive to viscosity and the wavelength becomes almost constant as in the inviscid case. This is because the viscosity damps short waves more strongly than long waves, and the damping effect weakens as Re increases. The decrease of λ/W_E with increasing horizontal shear observed in the weak horizontal shear range in Fig. 21, where Re is below 40, appears to be consistent with the results of Betchov and Szewczyk (1963). However, the remarkable increase of λ/W_E with increasing horizontal shear above that range appears to be quite curious. Shear instability waves attenuate with distance from the shear zone, with e -folding scales proportional to the wavelengths (e.g., Drazin and Reid 1981). Thus, for the Burgers vortex layer, long waves will feel more strongly the effect of the convergent cross-shear flow which increases linearly with the distance from the shear zone. Lin and Corcos (1984) showed that the most unstable wavelength for the Burgers

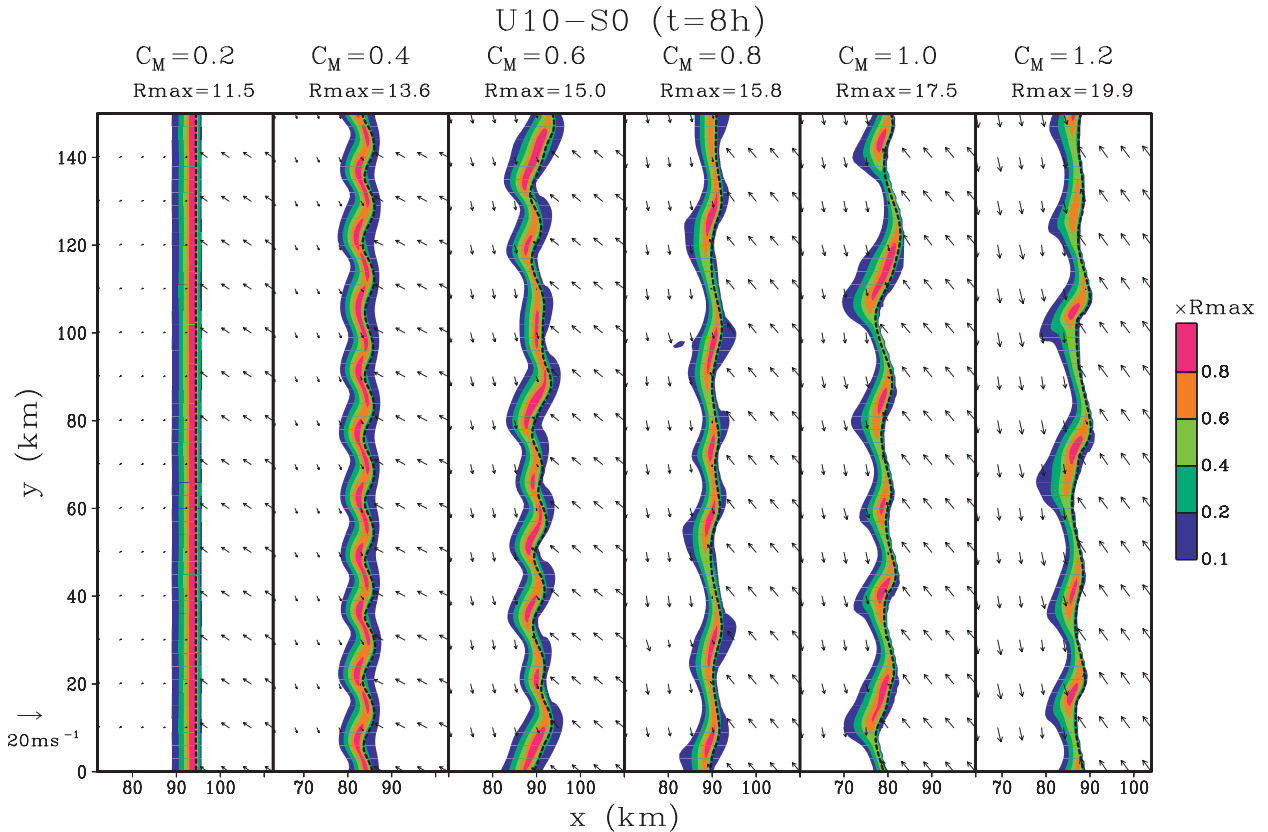


FIG. 20. As in Fig. 7, but for the U10-S0 horizontal shear experiments at $t = 8$ h. Only a $40 \text{ km} \times 150 \text{ km}$ portion of the full domain is shown.

vortex layer becomes somewhat shorter than that in the unstrained case described in Betchov and Szewczyk (1963) especially in small Re range. As discussed by Neu (1984), this is because the uniform plain convergence will act to stabilize long waves more strongly than short waves, in contrast to the viscosity. However, the dependency of the most unstable wavelength on Re shown in Lin and Corcos (1984) is qualitatively the same as that for the unstrained case (i.e., the effect of convergence only partially offsets the decreasing tendency of the wavelength with increasing Re). Considering the results of Lin and Corcos (1984), it is unlikely that the decrease in the magnitude of horizontal convergence relative to that of horizontal shear is responsible for the increase of λ/W_E with increasing horizontal shear observed in our simulations.

b. Effects of local vertical shear on scale selection

As shown in the previous section, the local vertical shear around the leading edge acts to suppress the growth of HSI waves. The local vertical shear increases with increasing distance from the location of maximum horizontal shear, associated with the increase of the frontal slope from the vertical (see Fig. 5). Thus, it is suggested

that the local vertical shear will stabilize long waves more strongly than short waves because long waves are less attenuated in the cross-frontal direction and, therefore, experience the effect of the local vertical shear more strongly than short waves.

To confirm the effect of local vertical shear proposed above and examine its dependency upon the horizontal shear strength, additional simulations are performed in which the wavelengths of AFV are specified by setting $\theta_{pv}(y) = 0.25 \sin(2\pi y/\lambda_p)$ in (9). The wavelength λ_p is varied from 4 to 40 km in increments of 2 km, and the model meridional domain size is set to λ_p . The specification of the initial wavelength makes the growth rate of the HSI wave in the early growth stage almost constant with time, which makes it possible to construct a dispersion curve.

Figure 22 shows the growth rates and the magnitudes of the volume-averaged VSP relative to that of HSP ($-VSP/HSP$) for the U10-S0 simulations utilizing $C_M = 0.4 \times 10^{-4}$, 0.8×10^{-4} , and $1.2 \times 10^{-4} \text{ s}^{-1}$. The growth rate σ was obtained by dividing the average change rate of the EKE for the middle 20 min of its exponential growth stage in half {i.e., $\sigma = (1/2)d[\ln(EKE)]/dt$ }, for which period $-VSP/HSP$ was also calculated. The magnitude of

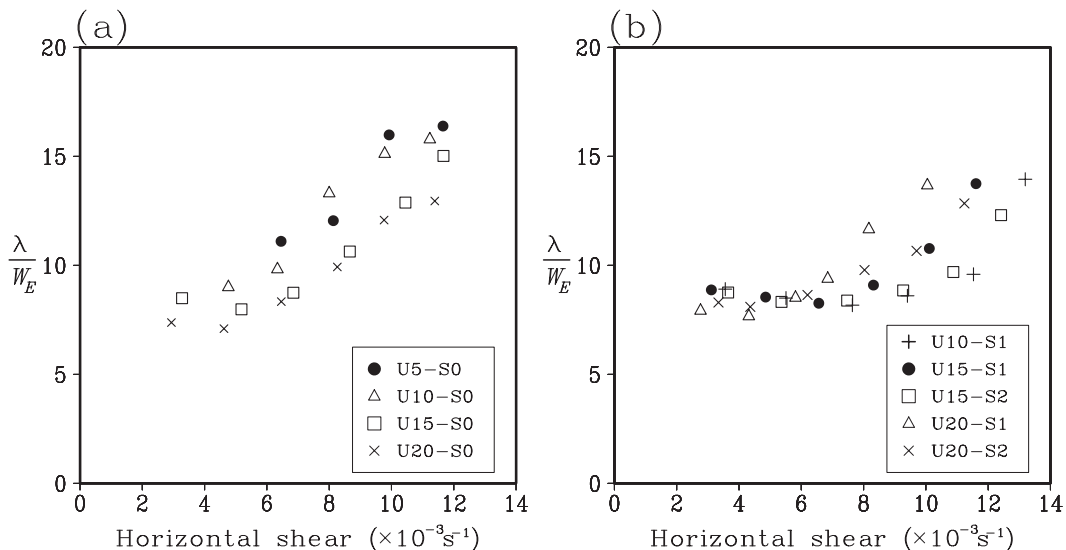


FIG. 21. Ratio of λ to W_E as a function of the horizontal shear strength. (a) Simulations initialized with the S0 sounding and (b) simulations initialized with the S1 and S2 soundings. Data for U5-S0 utilizing $C_M = 0.2 \times 10^{-4}$ and $0.4 \times 10^{-4} \text{ s}^{-1}$ and U10-S0 utilizing $C_M = 0.2 \times 10^{-4} \text{ s}^{-1}$ are not included because in each of these cases the growth of HSI waves was not observed.

–VSP/HSP provides a measure of the effect of local vertical shear on suppressing HSI waves. The growth rate is maximized at longer wavelengths for stronger horizontal shear simulations (Fig. 22a), consistent with the results shown in Fig. 21. On the other hand, –VSP/HSP increases with increasing wavelength (Fig. 22b), supporting the assumption that the local vertical shear will stabilize long waves more strongly than short waves. Furthermore, the value of –VSP/HSP for a given wavelength decreases as C_M increases, indicating that the stabilizing effect of local vertical shear decreases with increasing horizontal shear. This is because the magnitude of the local vertical shear of cross-front wind ($\partial\bar{w}/\partial z$) relative to that of the horizontal shear decreases as the horizontal shear increases. These results strongly suggest that the presence of local vertical shear and the decrease in its magnitude relative to that of the horizontal shear is responsible for the increase in λ/W_E with increasing horizontal shear.

Figure 23 shows the same variables as in Fig. 22 for the $U_S = 20 \text{ m s}^{-1}$, $C_M = 0.8 \times 10^{-4} \text{ s}^{-1}$ simulations initialized with the S0, S1, and S2 soundings. The peak of the growth rate curve shifts toward shorter wavelengths as the stratification becomes unstable (Fig. 23a), consistent with the stability dependency of λ/W_E noted in Fig. 21. The value of –VSP/HSP for a given wavelength increases as the stratification becomes more unstable (Fig. 23b). The increase of –VSP/HSP stems from the increases in the perturbation vertical velocity w' and the vertical Reynolds stresses. These results indicate that the stabilizing

effect of the local vertical shear on long waves increases as the stratification becomes more unstable. Thus, as the stratification becomes more unstable, stronger horizontal shear will naturally be required for a marked increase of λ/W_E to occur, as observed in Fig. 21.

Though not shown, additional simulations in which the strengths of heat and moisture sinks were varied indicated that increasing the temperature difference across the cold front in stably stratified cases has similar effect on the initial wavelength of an HSI wave as reducing the stability of stratification. This is probably because the local vertical shear of the cross-front wind and the strength of the vertical Reynolds stress increase as the temperature difference across the cold front increases.

6. Summary and conclusions

The sensitivity of AFV of wintertime maritime NCFRs to variations in various environmental characteristics have been investigated through a series of idealized simulations. In simulations initialized with a weak ambient cross-frontal vertical shear, the structures of the AFVs of NCFRs and their dependence on the stability of the prefrontal thermal stratification were found to be consistent with those described in K07, despite the differences in the frontal initialization method. In these cases, the AFVs of precipitation along NCFRs are attributed to wavelike disturbances within slanted frontal updrafts, which derive their energy mainly from the kinetic energy of mean local vertical shear and buoyancy. When the prefrontal

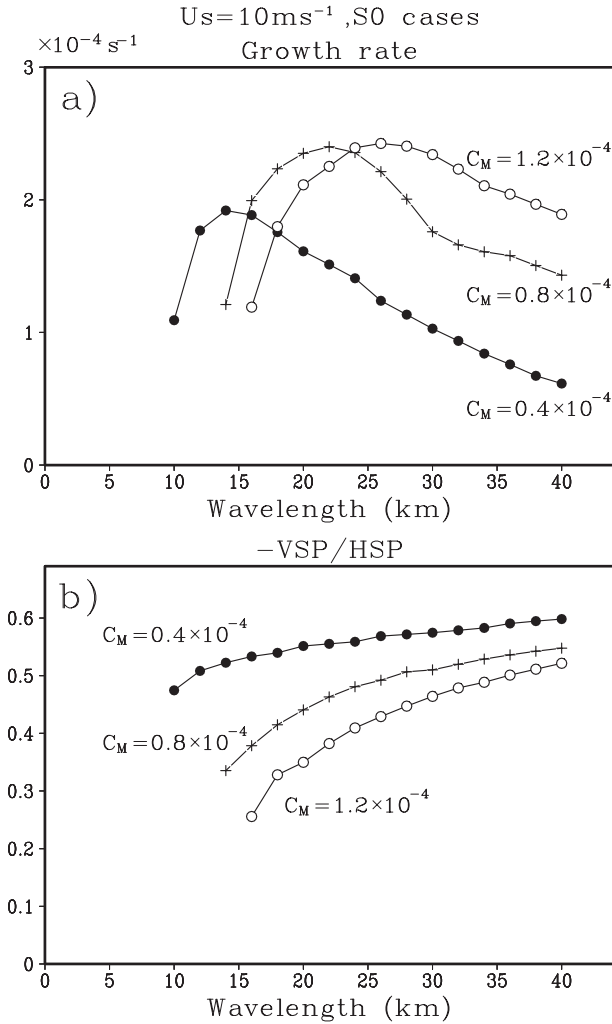


FIG. 22. Plots against the wavelength of (a) growth rates ($10^{-4} s^{-1}$) and (b) magnitudes of the domain-averaged VSP relative to that of HSP for the U10-S0 simulations utilizing $C_M = 0.4 \times 10^{-4}$ (closed circle), 0.8×10^{-4} (cross), and $1.2 \times 10^{-4} s^{-1}$ (open circle).

environment is slightly unstable, the wave phase lines are oriented nearly perpendicular to the direction of local vertical shear and PCs are aligned at a clockwise angle with respect to the cold front. As the prefrontal environment becomes sufficiently unstable, the wave phase lines become nearly parallel to the direction of local vertical shear and the PCs become oriented counterclockwise to the cold front.

On the other hand, the AFVs of NCFRs that are broadly consistent with previous observations occurred over a wider range of environmental conditions considered, including those of stable stratification, due to the development of HSI waves at the cold air leading edge. In relatively weak ambient vertical shear conditions, elongated PCs form along the segments of the SCF tilted

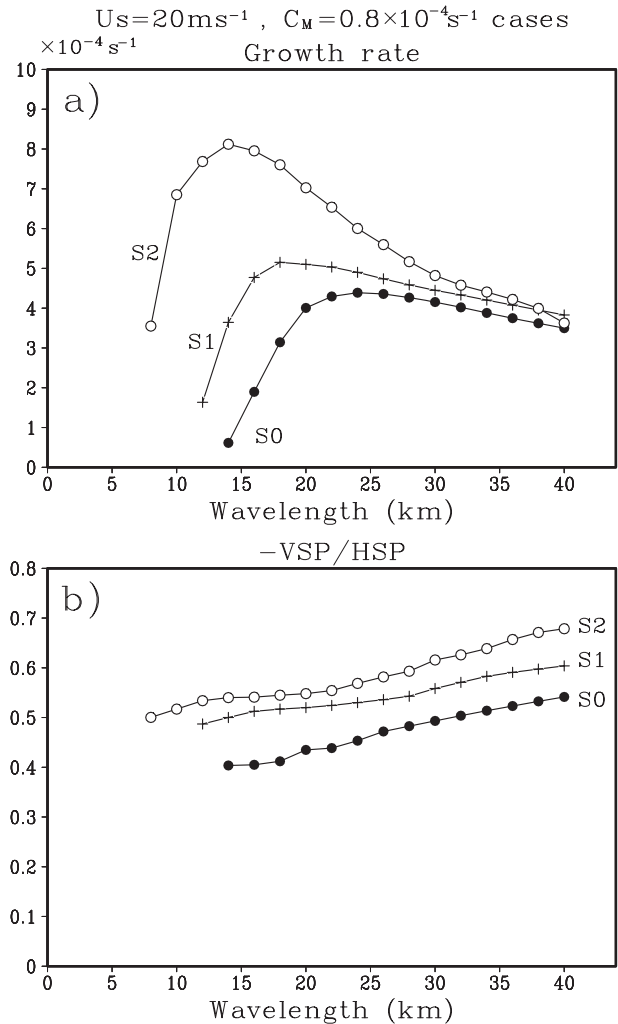


FIG. 23. As in Fig. 22, but for $U_s = 20 m s^{-1}$, $C_M = 0.8 \times 10^{-4} s^{-1}$ cases initialized with the S0 (closed circle), S1 (cross), and S2 (open circle) soundings.

clockwise from the general orientation of cold front, where the perturbed front makes largest angle with the low-level prefrontal wind and therefore the largest forced convergence occurs. On the other hand, in sufficiently strong vertical shear conditions, the precipitation along the NCFR tends to be organized into bow-shaped cores.

The growth rate and amplitude of the HSI wave decrease significantly as the ambient vertical shear of the cross-front wind is reduced, and the initial wavelength of the wave increases markedly with increasing horizontal shear. It is argued that the local vertical shear behind the leading edge causes these distinct dependencies of the HSI wave upon the vertical and horizontal shear strengths. The local vertical shear acts to damp the vorticity edge wave on the cold air side of the horizontal shear zone, thereby suppressing the growth of the HSI wave through the

interaction of two vorticity edge waves. The growth rate and amplitude of the HSI wave become small in weak ambient vertical shear conditions as a result of the enhancement of the local vertical shear. The local vertical shear is also shown to stabilize long waves more strongly than short waves. The marked increase of the initial wavelength with increasing horizontal shear is attributed to the decrease in the magnitude of the cross-front component of the local vertical shear relative to that of the horizontal shear.

The application of the results of this study to observations must be done with caution, since the environmental conditions for real NCFRs are considerably more complex and the parameters varied independently in this study are related to each other in a real cold front. It is hoped, however, that the information provided in this paper will help to interpret observations and more realistic simulations of NCFRs. The applicability of the results obtained for NCFRs to other boundaries possessing marked horizontal shear such as drylines, gust fronts, and dry cold fronts is largely debatable since those boundaries have rather different environmental characteristics (e.g., static stability, surface friction). The author thinks, however, that the discussions made in this paper may also contribute to the understanding of wave development along other boundaries, since NCFRs and other boundaries have similarities in their basic kinematic and thermodynamic structures.

Acknowledgments. This work was supported by the Grant-in-Aid for Scientific Research of the Ministry of Education, Culture, Sports, Science and Technology of Japan under Grant 21540446. The author would like to thank two anonymous reviewers for their helpful comments.

REFERENCES

- Adlerman, E. J., and K. K. Droegemeier, 2002: The sensitivity of numerically simulated cyclic mesocyclogenesis to variations in model physical and computational parameters. *Mon. Wea. Rev.*, **130**, 2671–2691.
- Arnott, N. R., Y. P. Richardson, J. M. Wurman, and E. M. Rasmussen, 2006: Relationship between a weakening cold front, mesocyclones, and cloud development on 10 June 2002 during IHOP. *Mon. Wea. Rev.*, **134**, 311–335.
- Atkins, N. T., R. M. Wakimoto, and T. M. Weckwerth, 1995: Observations of the sea-breeze front during CaPE. Part II: Dual-Doppler and aircraft analysis. *Mon. Wea. Rev.*, **123**, 944–969.
- Batchelor, G. K., 1967: *An Introduction to Fluid Dynamics*. Cambridge University Press, 516 pp.
- Betchov, R., and A. Szewczyk, 1963: Stability of a shear layer between parallel streams. *Phys. Fluids*, **6**, 1391–1396.
- Bishop, C. H., and A. J. Thorpe, 1994: Frontal wave stability during moist deformation frontogenesis. Part I: Linear wave dynamics. *J. Atmos. Sci.*, **51**, 852–873.
- Bretherton, F. P., 1966: Baroclinic instability and the short wavelength cut-off in terms of potential vorticity. *Quart. J. Roy. Meteor. Soc.*, **92**, 335–345.
- Browning, K. A., and T. W. Harrold, 1970: Air motion and precipitation growth at a cold front. *Quart. J. Roy. Meteor. Soc.*, **96**, 369–389.
- Bryan, G. H., 2005: Spurious convective organization in simulated squall lines owing to moist absolutely unstable layers. *Mon. Wea. Rev.*, **133**, 1978–1997.
- , and J. M. Fritsch, 2000: Moist absolute instability: The sixth static stability state. *Bull. Amer. Meteor. Soc.*, **81**, 1207–1230.
- , R. Rotunno, and J. M. Fritsch, 2007: Roll circulations in the convective region of a simulated squall line. *J. Atmos. Sci.*, **64**, 1249–1266.
- Carbone, R. E., 1982: A severe frontal rainband. Part I: Stormwide hydrodynamic structure. *J. Atmos. Sci.*, **39**, 258–279.
- Corcos, G. M., and F. S. Sherman, 1984: The mixing layer: Deterministic models of a turbulent flow. Part 1: Introduction and the two-dimensional flow. *J. Fluid Mech.*, **139**, 29–65.
- Drazin, P. G., and W. H. Reid, 1981: *Hydrodynamic Stability*. Cambridge University Press, 525 pp.
- Durrán, D. R., and J. B. Klemp, 1982: On the effects of moisture on the Brunt-Väisälä frequency. *J. Atmos. Sci.*, **39**, 2152–2158.
- Fovell, R. G., 1991: Influence of Coriolis force on two-dimensional model storms. *Mon. Wea. Rev.*, **119**, 606–630.
- , and Y. Ogura, 1989: Effect of vertical wind shear on numerically simulated multicell storm structure. *J. Atmos. Sci.*, **46**, 3144–3176.
- Friedrich, K., D. E. Kingsmill, and C. R. Young, 2005: Mesocyclone characteristics along Florida gust fronts during CaPE. *Mon. Wea. Rev.*, **133**, 3345–3367.
- , —, C. Flamant, H. V. Murphey, and R. M. Wakimoto, 2008: Kinematic and moisture characteristics of a non-precipitating cold front observed during IHOP. Part II: Alongfront structures. *Mon. Wea. Rev.*, **136**, 3796–3821.
- Fuhrer, O., and C. Schär, 2005: Embedded cellular convection in moist flow past topography. *J. Atmos. Sci.*, **62**, 2810–2828.
- Hane, C. R., 1973: The squall line thunderstorm: Numerical experimentation. *J. Atmos. Sci.*, **30**, 1672–1690.
- Heifetz, B., C. H. Bishop, and P. Alpert, 1999: Counter-propagating Rossby waves in the barotropic Rayleigh model of shear instability. *Quart. J. Roy. Meteor. Soc.*, **125**, 2835–2853.
- Hobbs, P. V., and K. R. Biswas, 1979: The cellular structure of narrow cold-frontal rainbands. *Quart. J. Roy. Meteor. Soc.*, **105**, 723–727.
- , and P. O. G. Persson, 1982: The mesoscale and microscale structure and organization of clouds and precipitation in midlatitude cyclones. Part V: The substructure of narrow cold-frontal rainbands. *J. Atmos. Sci.*, **39**, 280–295.
- Hoskins, B. J., M. E. McIntyre, and A. W. Robertson, 1985: On the use and significance of isentropic potential vorticity maps. *Quart. J. Roy. Meteor. Soc.*, **111**, 877–946.
- Houze, R. A., Jr., P. V. Hobbs, K. R. Biswas, and W. M. Davis, 1976: Mesoscale rainbands in extratropical cyclones. *Mon. Wea. Rev.*, **104**, 868–878.
- Iga, S., H. Tomita, M. Satoh, and K. Goto, 2007: Mountain-wave-like spurious waves associated with simulated cold fronts due to inconsistencies between horizontal and vertical resolutions. *Mon. Wea. Rev.*, **135**, 2629–2641.
- James, P. K., and K. A. Browning, 1979: Mesoscale structure of line convection at surface cold fronts. *Quart. J. Roy. Meteor. Soc.*, **105**, 371–382.

- Jorgensen, D. P., Z. Pu, P. O. G. Persson, and W.-K. Tao, 2003: Variations associated with cores and gaps of a Pacific narrow cold frontal rainband. *Mon. Wea. Rev.*, **131**, 2705–2729.
- Kawashima, M., 2007: Numerical study of precipitation core-gap structure along cold fronts. *J. Atmos. Sci.*, **64**, 2355–2377.
- Kirshbaum, D. J., G. H. Bryan, R. Rotunno, and D. R. Durran, 2007: The triggering of orographic rainbands by small-scale topography. *J. Atmos. Sci.*, **64**, 1530–1549.
- Lee, B. D., and R. B. Wilhelmson, 1997a: The numerical simulation of non-supercell tornadogenesis. Part I: Initiation and evolution of pretornadic mesocyclones circulations along a dry outflow boundary. *J. Atmos. Sci.*, **54**, 32–60.
- , and —, 1997b: The numerical simulation of non-supercell tornadogenesis. Part II: Evolution of a family of tornadoes along a weak outflow boundary. *J. Atmos. Sci.*, **54**, 2387–2415.
- , and —, 2000: The numerical simulation of non-supercell tornadogenesis. Part III: Parameter tests investigating the role of CAPE, vortex sheet strength, and boundary layer vertical shear. *J. Atmos. Sci.*, **57**, 2246–2261.
- Lilly, D. K., 1962: On the numerical simulation of buoyant convection. *Tellus*, **14**, 168–172.
- Lin, S. J., and G. M. Corcos, 1984: The mixing layer: Deterministic models of a turbulent flow. Part 3: The effect of plane strain on the dynamics of streamwise vortices. *J. Fluid Mech.*, **141**, 139–178.
- Lin, Y. L., R. D. Farley, and H. D. Orville, 1983: Bulk parameterization of the snow field in a cloud model. *J. Climate Appl. Meteor.*, **22**, 1065–1092.
- Lindzen, R. S., and M. Fox-Rabinovitz, 1989: Consistent vertical and horizontal resolution. *Mon. Wea. Rev.*, **117**, 2575–2583.
- Marquis, J. N., Y. P. Richardson, and J. M. Wurman, 2007: Kinematic observations of mesocyclones along boundaries during IHOP. *Mon. Wea. Rev.*, **135**, 1749–1768.
- Matejka, T. J., 1980: Mesoscale organization of cloud processes in extratropical cyclones. Ph.D. thesis, University of Washington, 361 pp. [Available from University Microfilms, 1490 Eisenhower Place, P.O. Box 975, Ann Arbor, MI 48106.]
- Moore, G. W. K., 1985: The organization of convection in narrow cold-frontal rainbands. *J. Atmos. Sci.*, **42**, 1777–1791.
- Murphey, H. V., R. M. Wakimoto, C. Flamant, and D. E. Kingsmill, 2006: Dryline on 19 June 2002 during IHOP. Part I: Airborne Doppler and LEANDRE II analyses of the thin line structure and convection initiation. *Mon. Wea. Rev.*, **134**, 406–430.
- Neu, J. C., 1984: The dynamics of stretched vortices. *J. Fluid Mech.*, **143**, 253–276.
- Parsons, D. B., 1992: An explanation for intense frontal updraft and narrow cold-frontal rainbands. *J. Atmos. Sci.*, **49**, 1810–1825.
- , and P. V. Hobbs, 1983a: The mesoscale and microscale structure and organization of clouds and precipitation in midlatitude cyclones. VII: Formation, development, interaction and dissipation of rainbands. *J. Atmos. Sci.*, **40**, 559–579.
- , and —, 1983b: The mesoscale and microscale structure and organization of clouds and precipitation in midlatitude cyclones. XI: Comparisons between observational and theoretical aspects of rainbands. *J. Atmos. Sci.*, **40**, 2377–2398.
- , C. G. Mohr, and T. Gal-Chen, 1987: A severe frontal rainband. Part III: Derived thermodynamic structure. *J. Atmos. Sci.*, **44**, 1615–1631.
- Pecnick, M. J., and D. Keyser, 1989: The effect of spatial resolution on the simulation of upper-tropospheric frontogenesis using a sigma-coordinate primitive-equation model. *Meteor. Atmos. Phys.*, **40**, 137–149.
- Persson, P. O. G., and T. T. Warner, 1991: Model generation of spurious gravity waves due to inconsistency of the vertical and horizontal resolution. *Mon. Wea. Rev.*, **119**, 917–935.
- Robe, F. R., and K. A. Emanuel, 2001: The effect of vertical wind shear on radiative-convective equilibrium states. *J. Atmos. Sci.*, **58**, 1427–1445.
- Rotunno, R., J. B. Klemp, and M. L. Weisman, 1988: A theory for strong, long-lived squall lines. *J. Atmos. Sci.*, **45**, 463–485.
- Smart, D. J., and K. A. Browning, 2009: Morphology and evolution of cold-frontal mesocyclones. *Quart. J. Roy. Meteor. Soc.*, **135**, 381–393.
- Snyder, C., W. C. Skamarock, and R. Rotunno, 1993: Frontal dynamics near and following frontal collapse. *J. Atmos. Sci.*, **50**, 3194–3212.
- Thorpe, A. J., M. J. Miller, and M. W. Moncrieff, 1982: Two-dimensional convection in non-constant shear. A model of midlatitude squall lines. *Quart. J. Roy. Meteor. Soc.*, **108**, 739–762.
- Wakimoto, R. M., and B. L. Bosart, 2000: Airborne radar observations of a cold front during FASTEX. *Mon. Wea. Rev.*, **128**, 2447–2470.
- , and H. V. Murphey, 2009: Analysis of a dryline during IHOP: Implications for convection initiation. *Mon. Wea. Rev.*, **137**, 912–936.
- Wang, P. Y., D. B. Parsons, and P. V. Hobbs, 1983: The mesoscale and microscale structure and organization of clouds and precipitation in midlatitude cyclones. VI: Wavelike rainbands associated with a cold-frontal zone. *J. Atmos. Sci.*, **40**, 543–558.
- Weckwerth, T. M., and R. M. Wakimoto, 1992: The initiation and organization of convective cells atop a cold-air outflow boundary. *Mon. Wea. Rev.*, **120**, 2169–2187.
- Weisman, M. L., J. B. Klemp, and R. Rotunno, 1988: Structure and evolution of numerically simulated squall lines. *J. Atmos. Sci.*, **45**, 1990–2013.
- Wilhelmson, R. B., and C.-S. Chen, 1982: A simulation of the development of successive cells along a cold outflow boundary. *J. Atmos. Sci.*, **39**, 1466–1483.
- Wilson, J. W., G. B. Foote, N. A. Crook, J. C. Fankhauser, C. G. Wade, J. D. Tuttle, C. K. Mueller, and S. K. Krueger, 1992: The role of boundary-layer convergence zones and horizontal rolls in the initiation of thunderstorms: A case study. *Mon. Wea. Rev.*, **120**, 1785–1815.